REVIEW

Detlef Diesing · Guido Kritzler · Matthias Stermann
Dirk Nolting · Andreas Otto

Metal/insulator/metal junctions for electrochemical surface science

Abstract We describe the preparation and characterization of Al-AlO$_x$-Ag tunnel junctions and calculate the energy distribution of the tunneling hot electrons in the range 0–2.5 eV above the Fermi level of silver. Because the mean free path of the hot electrons is of the order of the thickness of the silver film of the junction, which is at the same time the electrode in contact with an electrolyte, new surface effects can be studied. Hot electrons can be injected into the nonhydrated electron band in water. Hot electrons also cause hydrogen evolution at electrode potentials more positive than the ones needed in common electrochemistry. We observed the emission of hot electrons into silver during transients of hydrogen oxidation at silver and during oxidation of overpotential hydrogen on platinum clusters deposited on the silver electrode. The tunnel current at constant tunnel voltage can be changed by faradaic reactions, but surprisingly also by nonfaradaic reactions; this is assigned to a mesoscopic quantum phenomenon.

Keywords Tunneling in metal-insulator-metal structures · Electrochemical reactions induced by hot electrons · Hydrogen evolution and hydrogen reduction · Dependence of tunnel current on surface conditions · Sensorics

Introduction

The interface between a metal surface and an electrolyte solution is probably the most important electrochemical system. Driven by the potential difference at the metal/electrolyte interface a great number of reactions, such as charge transfer between the metal and a redox system at the electrode surface, metal deposition and dissolution,

D. Diesing · G. Kritzler · M. Stermann · D. Nolting · A. Otto (✉)
Lehrstuhl für Oberflächenwissenschaft (IPkM),
Heinrich-Heine-Universität Düsseldorf,
40225 Düsseldorf, Germany
E-mail: otto@uni-duesseldorf.de

corrosion and passivation, may occur. The potential difference as a driving force is built up by the solution side, which embraces the inner and outer Helmholtz plane and the Gouy–Chapman layer of the electrolyte, on the one hand, and the metal electrode with its ground-state electron distribution, on the other hand. The classical theories for the metal/electrolyte interface have concentrated for a long time on the solution side [1]. In modern theories, the electronic properties of the metal electrode, for instance, the extending tail of the electron distribution into the electrolyte, are included [2, 3]. It has been demonstrated that this spillover of the metal electrons into the solvent has an important effect on the interfacial capacity [4]. These and following works provided the initial understanding of how the electron distribution of the metal influences the electronic double layer [5]. Most of the newer theoretical models treat the electron gas (in its ground state) in the metal with the jellium model, where the interaction of the electron gas with the ions is simplified by smearing out the positive ionic charge into a background charge of constant density with a sudden transition to zero at the metal surface.

Dynamic changes of the previously mentioned electronic ground state of a metal surface are involved, for example, in surface electronic excitations [7], population of image states [8, 9], transient anionic [10] and cationic states of adsorbates [11] and bulk hot electrons and holes near the interface. These excitations or states are involved in one-photon processes, like photoemission (e.g., into the electrolyte [12, 13, 14, 15]) and nonadiabatic chemical reactions (e.g. desorption induced by electronic transitions [16, 17]), surface photochemistry [18, 19, 20, 21], also in the electrolyte [22], especially on silver [23], and in multiphoton processes such as non-linear surface optics (e.g. second-harmonic generation at ultrahigh vacuum, UHV, [24] and electrolyte interfaces [25, 26, 27]), two-photon photoemission (e.g. at UHV interfaces [28], and at electrolyte interfaces [29]), surface-enhanced Raman spectroscopy (SERS) at single-crystal electrodes [30], desorption induced by multiple electronic transitions [31], and light emission or manipulation

of individual molecules by a scanning tunneling microscope tip [32, 33].

In the work reported in Refs. [7, 8, 9, 10, 11, 12, 13, 14, 15, 16, 17, 18, 19, 20, 21, 22, 23, 24, 25, 26, 27, 28, 29] the hot electrons within the silver or at the silver surface were created by the interaction of "cold electrons" (electrons in the "Fermi sea" below the Fermi energy) with light. In the work reported in Refs. [32, 33] hot electrons were injected from the tunnel tip.

Electronic excitations at electrode surfaces by scanning tunneling microscopy have recently found interest [34, 35], but intensive investigations of electron transfer assisted by a tunnel process have already been done on thin oxide covered metal electrodes in so-called metal/ insulator/electrolyte (MIE) configurations [6, 36, 37, 38]. A schematic drawing of an MIE system is given in the upper part of Fig. 1 (taken from Ref. [6]). It shows an energetic model of an MIE system at equilibrium potential

$$E_{\text{redox}}(\text{solution}) = E_{\text{F}}(\text{metal}).$$

The reduction, for example, of Fe^{3+} in the solution by electrons tunneling through the metal oxide could be investigated in this configuration [6]. However it is not possible to control the energy of the tunneling electrons and the redox level of the redox species independently. This becomes possible in the metal 1/insulator/metal 2/ electrolyte (MIME) configuration (see the middle part of Fig. 1). In that system, a 20-nm-thick metal film (in our case silver or gold) acts as a working electrode (metal 2). The working electrode is separated by a 2-nm-thick oxide film from a second electrode metal 1 (in our case 30-nm-thick Al). By the application of a voltage between metal 1 and metal 2, a tunnel current flows through the oxide with hot electrons having an energy of $-e \cdot U_{\text{T}}$, where $U_{\text{T}} < 0$, above $E_{\text{F}}(\text{metal 2})$ at the oxide/metal 2 interface (see the middle part of Fig. 1). For intermediate voltages, $-3\,\text{V} < U_{\text{T}} < 0\,\text{V}$, a significant number (20–50%) of the tunneling electrons cross metal 2 almost elastically and hit the metal 2/electrolyte interface as hot electrons. There they can, for example, reduce oxidized species in the double layer (dotted arrow in the middle part of Fig. 1). On the other hand, the MIME configuration works as a detector for weak electronic interactions caused by nonequilibrium states in the double layer. In that case electrons (or holes) could be injected from the solution to the working electrode at energies different from $E_{\text{F}}(\text{metal 2})$. Then, the hot charge carriers can immediately be detected as a tunnel current in the tunnel junction (see the lower part of Fig. 1 at tunnel voltage zero.

By the injection of hot electrons into the working electrode the following relations to already established methods are revealed:

- Photoemission into the electrolyte/hot electron injection into the electrolyte (see later)
- Surface photochemistry at electrode surfaces/faradaic reactions with hot electrons (see later and Ref. [39]).
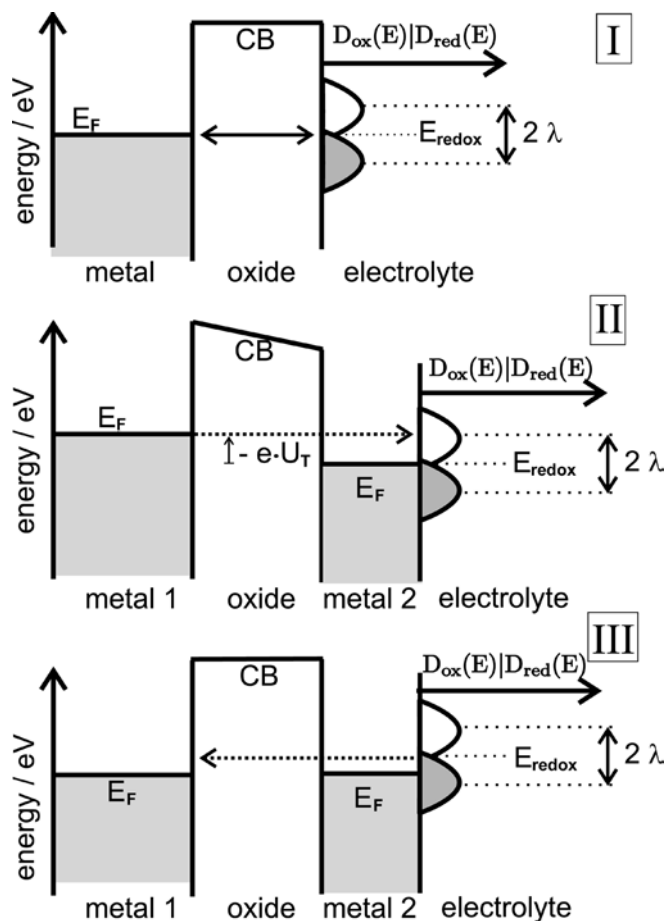

Fig. 1 *Top*: metal/metal oxide/electrolyte system at thermodynamic equilibrium potential (taken from Ref. [6]), λ being the solvent reorganization energy of the redox system in the electrolyte. *CB* is the lower edge of the conduction band in the oxide. *Middle*: metal 1/metal 1 oxide/metal 2/electrolyte system. Metal 2 is the working electrode at equilibrium potential with the redox system in the electrolyte. The application of a tunnel voltage U_{T} enables a hot electron transfer into the oxidized species (*dotted arrow*). *Bottom*: same system as in part II but not in an equilibrium state at the metal 2/electrolyte interface. Hot electron transfer from the solution side into metal 2 above $E_{\text{F}}(\text{metal 2})$ can be monitored as the tunnel current at zero tunnel voltage $U_{\text{T}} = 0\,\text{V}$

- Intermediate-charge transfer reaction in spontaneous SERS/optical surface absorption by charge-transfer excitations which can be observed as hot electron injection into the noble metal electrode of the MIM junction [40].

The linear surface optics with Al/ insulator/ silver/ electrolyte junctions were described in Ref. [41].

In the following sections we discuss the creation and transport of hot charge carriers by MIM junctions, and the preparation techniques and their influence on surface and bulk properties of MIM junctions, including the experimental setup, the characterization of the tunnel barrier, the energy distribution of hot electrons produced by the tunnel effect, the crystallographic orientation of MIM systems grown on glass substrates, the electrochemical setup and energy levels. Chemical reactions with

hot electrons are reported, including emission into the "dry electron", hydrogen evolution by hot electrons and hydrogen oxidation at silver surfaces, a model of the role of roughness in hot electron transfer, and redox reactions of hydrogen at platinum clusters on MIM junctions. The dependence of the internal current on the surface conditions of the top electrode, including cases without Faraday reactions, a model of the dephasing at the outer interface of an MIM junction and the modulation of the tunnel current by faradaic reactions are discussed. Sensorics with MIM junctions are also dealt with.

Creation and transport of hot charge carriers by MIM junctions

As shown in Fig. 1, tunnel junctions may act as hot electron sources. Later we show that the lower edge of the conduction band of the aluminium oxide layer is closer to the Fermi levels of two metal electrodes than the upper edge of the valence band of the aluminium oxide (see Fig. 10).

The exponential decays of the coherent wavefunction of tunneling electrons and holes in the insulating oxide layer are approximately controlled by the energy differences between the Fermi levels and the lower edge of the conduction band of the oxide. Thus, one may approximately apply models of tunneling through a vacuum gap (e.g. the Fowler-Nordheim model [42], taking the lower edge of the conduction band as the vacuum level ("conduction band tunneling").

MIM junctions allow electron and hole tunneling between the noble metal (in the following represented by silver) and the aluminium electrode according to the voltage $U_T = \Phi(Al) - \Phi(Ag)$, where Φ is the inner (or "Galvani") potential. In the electronic ground state and at negative (positive) values of U_T, electrons (holes) tunnel from aluminium into silver, where they may have the maximum positive energy $-e \cdot U_T$ with respect to the Fermi level of silver [so-called hot electrons (holes) in silver]. Note that the hot hole energy increases with the depth of the missing electron below E_F. We neglect inelastic tunneling, for instance, by excitation of phonons of the oxide, because its ratio with respect to elastic tunneling is very small.

One may also create hot electrons or holes in the silver electrode of the MIM junction by external means, for instance, by photon absorption [40] and electrochemical reactions at the silver electrolyte interface [43]. In this case observes a tunnel current at $U_T = 0$. There is a possibility to measure these extra currents as function of U_T (separation from the direct current owing to ground-state tunneling is possible with lock-in methods) and apply the junction as an internal retarding field energy analyzer of the externally exited hot carriers. As yet some problems remain in using MIM as internal retarding field spectrometers, see Ref. [40], but at small excitation energies and small retardations this method works well (see later and Ref. [43]).

Within the free-electron model, hot electrons and hot holes of low energy have the same mean free path [44]. The possible hot electrons and hole states within the silver top electrode are given by the electronic band structure of silver. In the tunneling and ballistic transport processes towards or off the silver/electrolyte interface the direction of propagation of the electronic wavepackets with respect to the surface normal depends on the orientation of the silver electrodes [e.g. (111) or (110) or (100) crystallographic planes parallel to the interface]. The projected density of electronic states is given in Fig. 18.

For the (111) orientation there is a gap in the range of the hot electrons between 0 and about 4 eV excitation energy. In this case, ballistic electrons have a minimum finite momentum parallel to the interface, and therefore propagate only above a finite limiting angle with respect to the surface normal. This was impressively demonstrated in real-space simulations by Borisov et al. [45] for the time-resolved emission of a hot electron at a noble metal (111) surface. This point will become important in understanding the hydrogen evolution reaction (HER) by hot electrons, see later. In contrast, one can expect propagation of hot electrons perpendicular to the surface ("on the shortest way between silver and aluminium") for a (110) orientation [40].

Usually a ballistic model is adopted for the hot electrons [46], separated in several independent steps:

- Tunneling of the electron from the aluminium into the silver, or, in the Fowler-Nordheim case, tunneling from the aluminium in the tilted oxide conduction band and transport within this band to the oxide/silver interface.
- Ballistic transport of the electron after tunneling (so-called primary hot electron) to the outer silver surface.
- Reaction of the primary hot electron at the surface.

This "ballistic aspect" (see the Monte Carlo simulations by Schaak in Refs. [47]) is complemented by the unexpected aspect of the breaking of the coherence of the electronic tunneling state at the interface which allows the variation or even control of the tunnel current between aluminium and noble metal electrode at constant tunnel voltage by changes at the noble metal interface (see later and Ref. [47]).

The electron–electron interaction will create a cascade of secondary hot electrons, mainly energy less than half of the energy of the primary electron [47], for which the participation in hot electron chemistry is expected [48]. We discuss in any case whether secondary hot electrons contribute to the observed phenomena later.

Preparation techniques and their influence on surface and bulk properties of MIM

Experimental setup

The preparation methods of tunnel junctions contain a wide range of physical and chemical methods [49].

Widely used are systems containing aluminium/aluminium oxide layers where the experiments are performed in UHV at low temperatures [50, 51]. The advantages of aluminium oxide are a considerably high specific resistance of 10^{13} Ωcm which is combined with the extremely small diffusion of oxygen or water (growth rate of the oxide film of less than 10 pm day^{-1} [52]). When tunnel junctions are transferred to the atmosphere or even to an electrochemical environment, the corrosion resistance and long-term stability play an important role. The production of stable junctions is discussed intensively in Refs. [41, 49]. Here we give only a short description of the preparation methods.

The Al film is evaporated in a high vacuum chamber with a pressure of 5×10^{-8} Torr. The "localised" anodic oxidation is performed in a droplet cell. The capillary contains the electrolyte (acetate buffer, pH 6.0) and a gold wire, which works as a counterelectrode. Details are given in Refs. [53, 54, 55]. The evaporated Al film is contacted with a gold wire. The localized anodization of Al films opens the possibility of programming the oxide structures. Another advantage is the reduction of stress in the Al film because only the junction area needs to be oxidized.

After the oxide formation, a 20-nm-thick silver film is evaporated as the top electrode and 30-nm-thick silver strips are evaporated for contacting the top electrode. A drawing of the layer ensemble can be seen in Ref. [56]. The resulting MIM sandwich structure has a capacity of 5 μF cm^{-2} for an oxide thickness of 2.5 nm. This means a dielectric constant of 12 for the oxide.

Characterization of the tunnel barrier

For the characterization of the tunnel barrier exact information about the difference between the Fermi level of the base metal and the conduction band of the oxide, on the one hand, and the Fermi level of the top metal and the conduction band of the oxide, on the other hand, is needed. These parameters and the oxide thickness are important for the tunneling probability in MIM junctions [57]. For an exact determination of the energy levels in the junction we used the mechanism of Fowler-Nordheim tunneling [42]. Fowler and Nordheim mentioned that the effective length of a tunnel barrier is reduced when a certain threshold voltage is reached, so tunneling electrons may partly use a conduction band state during tunneling. This effect is shown in Fig. 2. On the left of Fig. 2, the lower edge of the conduction band at the oxide/aluminium interface just reaches the Fermi level of the Ag. In this case the energy $e{\cdot}U_T$ of the tunneling electrons above the Fermi level of Al is equal to the difference $E_{CB}(oxide) - E_F(Al)$, where $E_{CB}(oxide)$ means the lower edge of the conduction band at the Al/oxide interface.

When the Fermi level of the Al is further lowered by applying a more positive tunnel voltage to the Al electrode, the tunneling electrons use partly the conduction
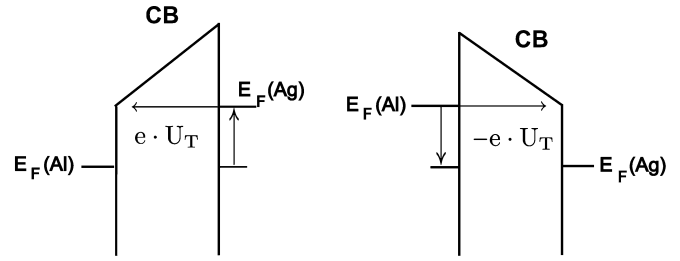

Fig. 2 Energy levels in metal/insulator/metal (*MIM*) junctions in the case of starting Fowler-Nordheim tunneling ($|e{\cdot}U_T| = |E_F(Ag) - E_F(Al)|$). *Left*: ($U_T > 0$), electrons tunnel into the Al electrode, equivalent to hot hole injections into silver. *Right*: ($U_T < 0$) hot electron injection into the Ag electrode, equivalent to hot hole injection into aluminium. It is assumed that the Ag electrode is always at ground level, see Fig. 9. The energetic position of the Fermi level of the silver does not change

band for tunneling through the oxide. This reduces the effective length of the tunnel barrier.

The tunnel current depends exponentially on the tunnel voltage and the effective length of the tunneling barrier. A logarithmic plot of the tunnel current versus the tunnel voltage reveals possible changes in the effective tunnel length known as the Fowler-Nordheim mechanism.

The tunnel current is plotted with a logarithmic scale versus the tunnel voltage for an MIM junction with 2.4-nm anodic oxide in Fig. 3. At a tunnel voltage $U_T = 2.4$ V the slope of the logarithmic plot increases, indicating enhanced tunnel probability at tunnel voltages $U_T > 2.4$ V, see Fig. 3. We assign this enhanced tunneling probability to the reduction of the effective tunnel length as shown on the left of Fig. 2 due to the band edge E_F (Al) /anodic oxide of 2.4 eV. By applying a negative tunnel voltage (left-hand side of Fig. 3), we obtain the corresponding information on the band edge of the anodic oxide/silver interface. The slope of the logarithmic plot increases at $U_T = -3.9$ V, indicating an E_F (Ag)/ anodic oxide band edge of 3.9 eV following the mechanism on the right of Fig. 2.

It should be mentioned that the temperature dependence of the tunnel currents is quite low (increase of 20%) between 40 and 200 K. This fact will be exploited in Fig. 4.

In order to support the previously mentioned assignment of the slope changes in Fig. 3 we calculated the current voltage plots exactly by the assumption of an asymmetric trapezoidal barrier considering also the image potential with $\epsilon_{relative} = 12$ for the oxide. The onset of the Fowler-Nordheim tunneling can be derived exactly. When the relation

$$\frac{\partial^2 \log(I_T)}{\partial U_T^2} = 0 \tag{1}$$

is fulfilled for a certain tunnel voltage U_T, the energy $|e{\cdot}U_T|$ corresponds to either conduction band (oxide)–$E_F(Ag)$ or conduction band (oxide)–$E_F(Al)$.

Fig. 3 Current–voltage plot (current axis with logarithmic scale) of the MIM junction in an ultrahigh vacuum with anodic oxide at 42 K (Beginning of Fowler-Nordheim tunneling indicated by *vertical arrows*)
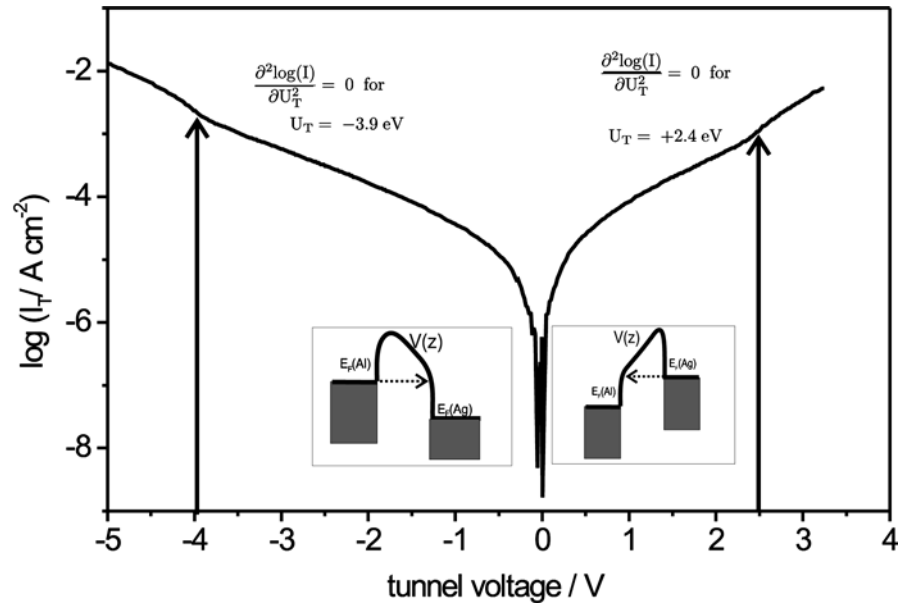
In Fig. 4 the logarithmic current voltage plots are given for another MIM junction at 42 K for both current directions through the oxide (see also the insets in Fig. 4). The tunnel voltage was scanned with a rate of 0.1 V s^{-1} 200 times for 42 and 200 K. The ratios of both of the 200 scans at 42 and at 200 K are given as a scatter graph inserted with a second y-axis in Fig. 4.

Exceptional values, for example, owing to current spikes in the 200 K curve, are not shown here. The small crosses in the figure give the main trace of the ratio. A pronounced increase in the ratio of the currents at $U_T = 2.4$ V and $U_T = -4.0$ V can be seen. At these voltages a change in the slope of the current voltage plot also appears (Fig. 4). One can understand the enhanced current increase at these voltages by the assumption that our oxide barrier is asymmetric with barrier heights of $\varphi_1 \approx 2.4$ eV and $\varphi_2 \approx 4.0$ eV. During heating from 42 to 200 K a bigger fraction of electrons tunnels through the barrier, whose length is shortened by the onset of the Fowler-Nordheim tunneling. Thereby the tunnel current increases much more at voltages $|e \cdot U_T| = \varphi_1, \varphi_2$ than at other voltages.

The calculation of the temperature dependence of a direct elastic tunnel current for barrier heights of 1.0 and 1.5 eV was done by Simmons [58] based on the Wentzel-Kramers-Brillouin (WKB) approach for 2-nm-thick barriers. Since our tunnel barriers are only 20% thicker but 2.4 and 4.0 eV much higher than the ones of Simmons, a computation with the WKB-approach is not appropriate. A significant part of the electron tunneling path does not fulfill the WKB criterion in our tunnel barriers; therefore, we performed a pure numerical solution of the Schrödinger equation omitting the WKB approach.

The calculation is based on the absolute tunnel current density [59]

$$i_{\text{tunnel}} = \frac{2e}{\hbar} \int_0^\infty \mathrm{d}E \cdot \int_0^\infty \frac{\mathrm{d}^2 k_{||}}{(2\pi)^2} \cdot [f(E,T) - f(E + e \cdot |U_T|, T)] \cdot D(E, k_{||}). \tag{2}$$

$f(E,T)$ denotes the Fermi distribution at temperature T, $k_{||}$ the momentum of the tunneling electrons parallel to the barrier. $D(E,k_{||})$ is the transmission factor of the oxide barrier (for electrons at energy E and momentum $k_{||}$) and is achieved by an ab initio solution of the Schrödinger equation. For the solution of the Schrödinger equation we follow a numerical procedure which was set up by Politzer [60].

For $V(z)$ an image-potential-corrected ($\epsilon = 12$ [49]) asymmetric barrier with the previously mentioned barrier heights was taken. The calculated ratio of tunnel currents at two different temperatures (42 and 200 K) as a function of the applied tunnel voltage is shown in Fig. 5. The calculated curves also show a maximum at the tunnel voltages corresponding to the onset of the Fowler-Nordheim tunneling as one would expect intuitively.

The clearly enhanced temperature dependence of the experimentally found tunnel current (Fig. 4) in the Fowler-Nordheim case shows that the direct elastic tunnel process is dominant in the present case. If the main conduction mechanism for the anodic oxides were a hopping-dominated conduction, no pronounced enhancement of the temperature dependence should be expected in the Fowler-Nordheim case.

Finally, one can say that our previous assignment of the slope changes in the logarithmic current plot to the onset of the Fowler-Nordheim tunneling is well corroborated.

A short overview of our work on aluminium thin film based tunnel junctions with differently prepared oxides is given in Fig. 6.
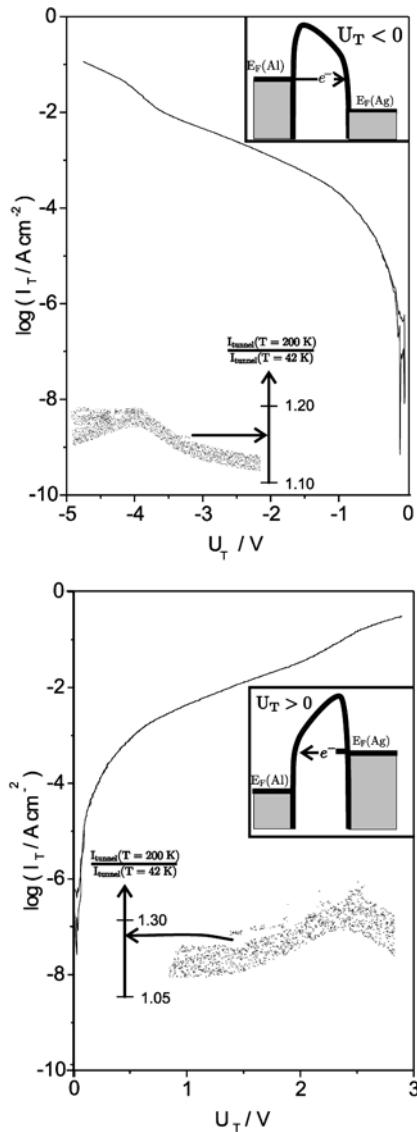
Fig. 4 Measured current–voltage plot for an aluminium/2.3-nm anodic oxide/silver system at 42 K. Current axis logarithmically scaled. Second *y*-axis: individual ratios of tunnel currents $\frac{i_T(T=200K)}{i_T(T=42K)}$ as a function of U_T for 200 scans

Fig. 5 Calculated ratio of tunnel currents $\frac{i(200K)}{i(42K)}$ for direct elastic electron tunneling through an asymmetric trapezoidal barrier with barrier heights $\varphi_1 = 2.4$ eV and $\varphi_2 = 3.9$ eV and $\epsilon_{oxide} = 12$. *Insets*: conditions for the onset of Fowler-Nordheim tunneling

Some comments should be added on the strong asymmetry of the tunnel barriers used in this work.

Neglecting chemical bonds and dipole layers between the metals and the oxide, the asymmetry should be induced by the difference of the work functions of the two metals. Since $\Phi_{Al} = 4.25$ eV and $\Phi_{Ag} = 4.3$ eV [61], a nearly symmetric barrier should be expected. This is not even the case for MIM junctions with gas-phase oxide layers where the asymmetry and, thereby, the flat band potential is 0.5 eV. The asymmetry is increased towards 1.5 eV for anodic oxide films as insulators. The corresponding flat band potential of 1.5 eV may be explained by an interfacial dipole layer at the oxide/silver interface; this exists even in the gas-phase oxide samples and is increased in the anodic oxide samples. This coincides with the tunnel junction investigations of Hickmott [62],
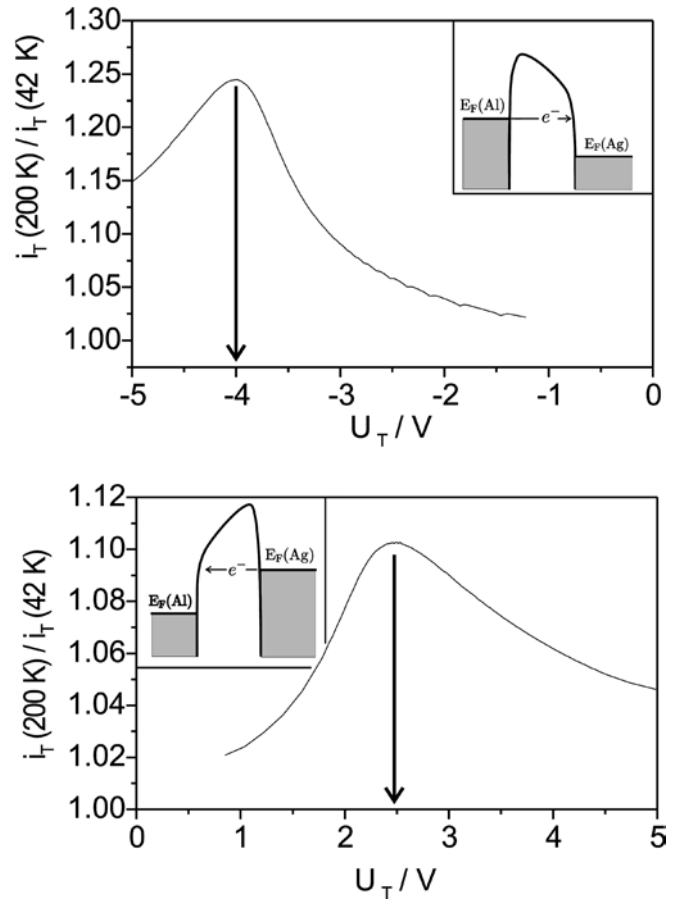
who found indications for interface states in tunnel junctions by impedance spectroscopy.

Energy distribution of hot electrons produced by the tunnel effect

The main scope of our present work is the investigation of chemical processes induced by the hot electrons tunneling from the aluminium through the oxide to the silver/adsorbate or to the silver/electrolyte interface. A proposal for this kind of hot electron chemistry was made by Gadzuk [48]. He mentioned the monochromatic properties of such kinds of electron sources. For our steep and thin oxide barriers this had to be checked again.

From the exact shape of the tunnel potential, $V(z)$, which we derived in the previous subsection, we can derive the exact shape of the energy distribution of hot electrons which are injected into the top metal. One has to take into account the Fermi distribution, $f(E,T)$, of the electron source (aluminium) at room temperature and the transmission factor of the tunnel barrier, $D(E,k_{\parallel})$. This product is plotted in Fig. 7 for two tunnel

Fig. 6 Offsets of the lower boundaries of the AlO$_x$ conduction band from the Fermi levels in three differently grown MIMs, obtained from the values of U_T at which $\partial^2[\log(I_T)]/\partial U_T^2 = 0$ is fulfilled. *Top*: offset at the Ag/AlO$_x$ interface. *Bottom*: offset at the Al/AlO$_x$ interface
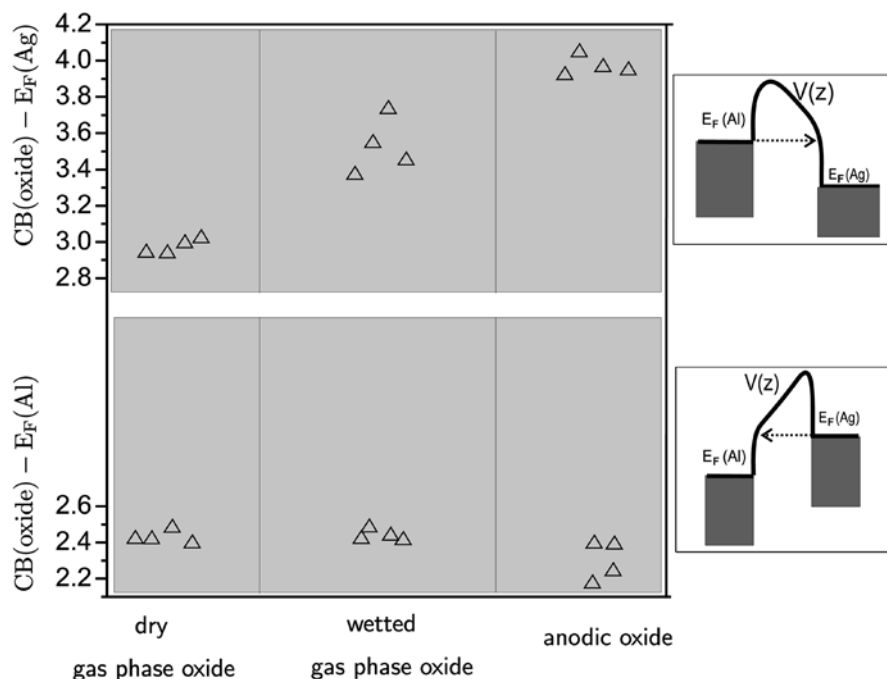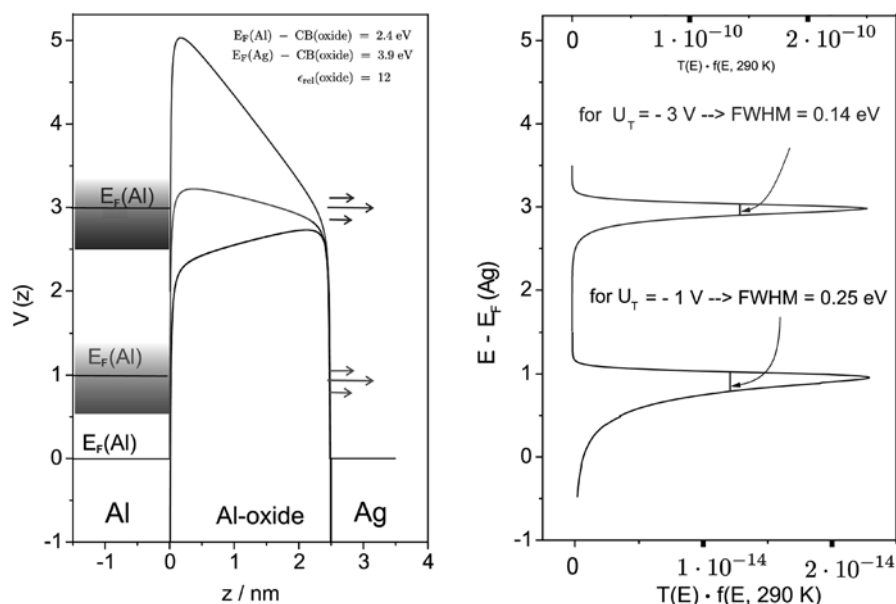

Fig. 7 *Left*: cross section of the MIM system and the barrier $V(z)$ with different tunnel voltages $U_T = -1$ V and $U_T = -3$ V. *Right*: distribution of hot electrons [product of transmission factor of the tunnel barrier $T(E)$ and the Fermi distribution of the Al $f(E)$] which are injected into the top metal electrode (silver). *Upper* (*lower*) *curve* with upper (lower) scale

voltages ($U_T = -1$ V, lower curve, and $U_T = -3$ V, upper curve). The electron distribution injected into the silver film shows a considerable width of 0.25 eV at room temperature and $U_T = -1$ V which decreases considerably for higher tunnel voltages (0.14 eV for $U_T = -3$ V).

The often-mentioned monochromatic properties of this type of hot electron source has therefore to be considered with respect to the applied tunnel voltage.

Note that the calculations for Fig. 7 did not take into account the finite thicknesses of the Al and Ag films of the junction. As the experiments described later demonstrate the finite thickness leads to new effects, by which the tunnel current is not only given by the shape

of the barrier and the band structure of the metals, but is controlled "from outside"(e.g. from the electrolyte). We try to explain this qualitatively later.

Crystallographic orientation of MIM systems grown on glass substrates

The crystallographic orientation of the top metal electrode can be obtained by the Bragg-Brentano method of X-ray scattering. The method delivers a signal from those lattice planes which are parallel to the macroscopic plane of the film. Of course, this method is applicable to

the top electrodes of MIM junctions. The spectrum in Fig. 8 shows an MIM junction grown on glass slides. A preferentially (111) orientation with presumably azimuthal randomness can be seen with a small fraction of (100) orientation. Owing to the limited penetration depth and the amorphous structure of the oxide all the discrete features in the X-ray spectrum can be assigned to the silver top electrode. Therefore the present work is focused on hot electrons in Ag(111) films. This is especially important for the discussion of the influence of surface roughness on the transfer of hot electrons into the adsorbates (see later).

Electrochemical setup

Electrons with an energy of some electron volts above the Fermi energy of silver, so-called hot electrons, are created in Al/aluminium oxide/Ag tunnel junctions by application of a negative voltage between the Al and the Ag electrode (see Fig. 2 right side and Fig. 10).

In the electrochemical setup (Fig. 9) the silver film of the MIM is connected as the working electrode in an electrochemical cell. Especially important for the present work is the shift of the electronic levels within the bulk electrolyte, for example, the dry electron mentioned earlier. The experiments were carried out in highly concentrated electrolytes ($c > 5 \times 10^{-2}$ M). We can assume that a potential change of x eV moves the levels in the electrolyte also by x eV. To perform these
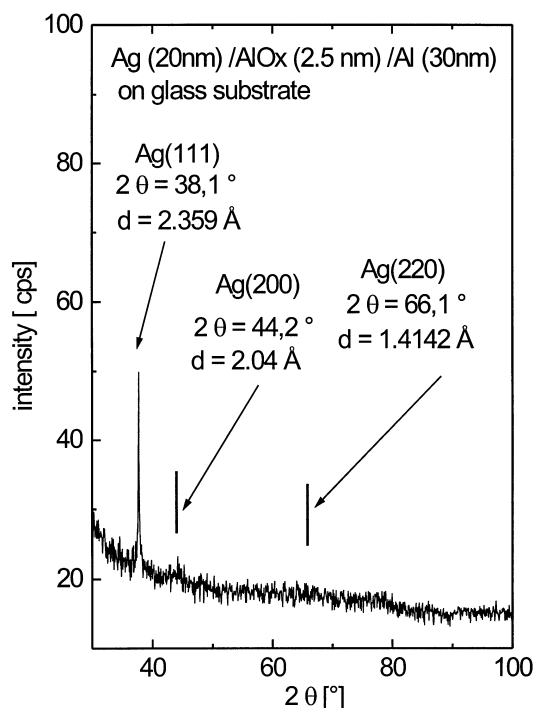
measurements two electrical circuits are necessary (Fig. 9). One circuit contains the voltage source and the ampere meter to control the current, I_T, through the tunnel junction. The other circuit controls the electrode potential, E_{SCE}, of the silver or gold top electrode of the MIM junction which is connected as the working electrode and acts as a common ground for both circuits. The counterelectrode is a platinum wire. As a reference we chose the saturated calomel electrode. The active tunnel area of the samples is typically 0.12 cm^2 and is in contact with the electrolyte. Outside this area the sample is covered with a protective lacquer. In order to improve the stability of the MIM junctions we had to chose 50% water and 50% ethylene glycol electrolytes rather than pure aqueous electrolytes.

Energy levels

Now a complete energy level scheme for the MIM junction in contact with an electrolyte can be derived, for example, at $U_T = -2.2$ V, see Fig. 10).

In the electrochemical setup, the silver top electrode is used as a working electrode in an electrochemical circuit. The working electrode is the common ground of the "electrochemical" and the "tunnel" circuit. The potential of the working electrode is applied by changing the potential of the counterelectrode, which is a Pt wire.

On the left-hand side of Fig. 10 the potential scales are given with respect to the Fermi level of silver, which is our working electrode. The working electrode is in equilibrium with an electrolyte at the potential $E_{SCE} = 0.0$ V (see potential scale on the right-hand side of Fig. 10). On that potential scale, the onset of photoemission (transfer of a photoexcited electron to the solution) is at $E_{SCE} = -3.48$ V, see, for example, also Fig. 4 in Ref. [65]. On the same scale the transfer of an electron from a redox couple to the vacuum would occur at $E_{SCE} = -4.62$ V (see, for example, Eq. 2 p. 367 in Ref. [38]). However, it should be noted that at a metal

Fig. 8 X-ray diffraction versus scattering angle 2θ of a tunnel junction with Ag top electrode. The positions of the possible reflexes are indicated. d is the distance between lattice planes yielding the Bragg reflections indicated
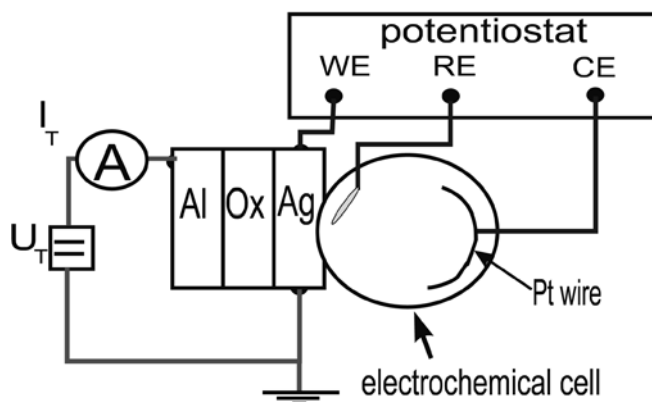

Fig. 9 Tunnel junction in electrochemical circuit. *WE*: working electrode, *CE*: counter electrode = platinum wire, *RE*: reference electrode = saturated calomel electrode. U_T: tunnel voltage, I_T: tunnel current
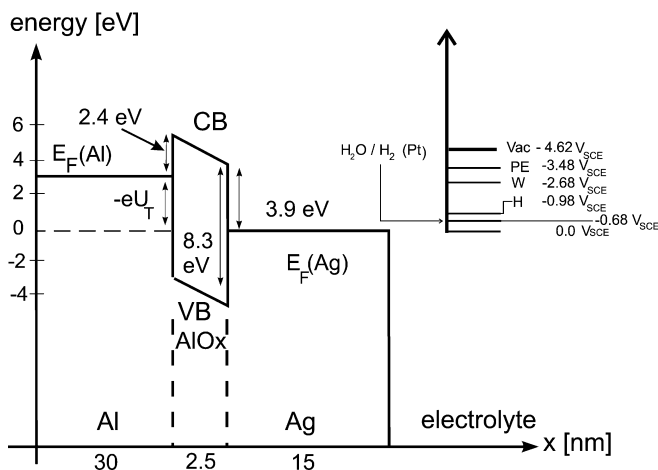
Fig. 10 Energy scheme of the tunnel junctions (eV) in contact with the electrolyte. *PE* is the lower edge of the electron conduction band in the electrolyte (= D state in Ref. [63], so-called dry electron). The HER from water at a platinum electrode in 0.9 M acetate buffer(pH 5.9) with 50% water and 50% ethylene glycol electrolyte [56] takes place at $E_{SCE} = 0.68$ V. The position of the lower edge *W* of the so-called wet electron state and the centre *H* of the hydrated state of the electron in an aqueous electrolyte [63], all levels at the electrochemical potential of the top silver electrode of 0 V_{SCE}. (In this case the Fermi levels of the silver electrode and of the metallic mercury in the saturated calomel electrode, *SCE*, $E_F(SCE)$ are at the same level). 1 eV on the energetic scale corresponds to 1 V_{SCE} on the electrochemical potential scale. *CB*: lower edge of conduction band of Al_2O_3. *VB*: upper edge of valence band. U_T: tunnel voltage (the silver electrode is at ground level). The vacuum level is at $E_{vacuum} = -4.38\ V_{NHE} = -4.62\ V_{SCE}$ [64]. Band offsets are for tunnel junctions with anodic oxide, see Fig. 5.

electrode, the electrode potentials of the experimentally observed onsets of charge–transfer reactions (e.g., the photoemission into the electrolyte) can be referenced to the Fermi level of the metal directly without applying the concept of the two further interfaces, the electrolyte/vacuum and the metal/vacuum interface, or in other words the position of the vacuum level above the potential of the reference electrodes and the work function of the metal. This detour is only necessary at semiconductor electrodes; in the metal case it may lead to considerable errors, see, for instance, the discussion in Ref. [66].

In Fig. 10 the two hydrated states of the electron are inserted, the electronic p state, called the wet electron (W) and the electronic s state, called the H state. Their position is fixed in Fig. 10 by the experimental value (PE) of the photoemission into the electrolyte and the position of W and H with respect to PE inferred from the time-resolved dynamics of hydration [63]. It should be noted that under normal conditions an electron cannot be transferred directly to the hydrated states W and H. H is the stable ground state from which the electron may be scavenged by special molecules in the solution or eventually return to the electrode [67]. For the hot electron energies below 4 eV and transfer into states above PE, outside the Helmholtz layers, one can safely exclude any chemical reaction with water. The lowest electron energy necessary to dissociate water is

6.5 eV in the gas phase [68] and 5.5 eV in six amorphous monolayer films of water on a platinum substrate [69].

Of course reactions by the transfer of electrons to species inside the Helmholtz layers, for instance, the HER, do not need the detour via PE and can take place at electrode potentials nearer to 0 V_{SCE}, see, for instance, the onset of the hydrogen evolution H_2O/H_2 at $-0.64\ V_{SCE}$ in Fig. 10. The potential scale on the right-hand side of Fig. 10 additionally shows the experimentally found onsets of the HER at polycrystalline platinum surfaces ($E_{SCE} = -0.68$ V).

The onset potentials of the HER on electrode surfaces in the electronic ground state and in electronically excited states (induced by the injection of hot electrons) is discussed further later.

Chemical reactions with hot electrons

Emission of hot electrons into the "dry electron" state

Immediately after emission of the photoelectron from the metallic electrode into the electrolyte the permanent dipoles of the water molecules are not yet rotated by the photoelectron. The delocalized state is called the "dry electron state". The lowest dry electron state constitutes the lower edge of the electronic conduction band of water. This threshold for photoemission [70] is called PE in Fig. 10. The solvated electronic states cannot be reached directly by photoemission. The following values for PE can be found in the literature: $-3.4\ V_{SCE}$ [12], $-3.3\ V_{SCE}$ [71], $-3.26\ V_{SCE}$ [72], $-3.23\ V_{NHE}$ [14].

Körwer [73] found 3.44 V_{SCE} for polished polycrystalline silver electrodes by photoemission. In the common electrochemistry with the silver electrode in its electronic ground state the injection of electrons into PE would start only at an electrode potential of $-3.48\ V_{SCE}$, far in the potential range of the hydrogen evolution which starts below about $-1.2\ V_{SCE}$, see curve b in Fig. 13. Thus, this injection is unobservable. However, a transfer to PE without interference of the common hydrogen evolution is possible by tunnel junctions, which was shown first by Diesing [74, 75] on silver electrodes.

The electrode current is plotted as a function of the tunnel voltage for different electrode potentials in Fig. 11. One can observe, for example, for $E_{SCE} = -0.8$ V a sharp increase in the cathodic current at $U_T = -2.5$ V. Comparing the different curves in Fig. 11 delivers two aspects:

- At an electrode potential of $E_{SCE} = -0.2$ V it is not possible to influence the electrode current by tunnel voltages $U_T > -3.0$ V.
- The curve at $E_{SCE} = -0.8$ V is shifted with respect to the curve at $E_{SCE} = -0.7$ V by 110 mV tunnel voltage U_T in a negative direction.

When one plots the tunnel voltage where the cathodic current starts (Fig. 11), versus the electrode potential, one obtains the dots in Fig. 12.
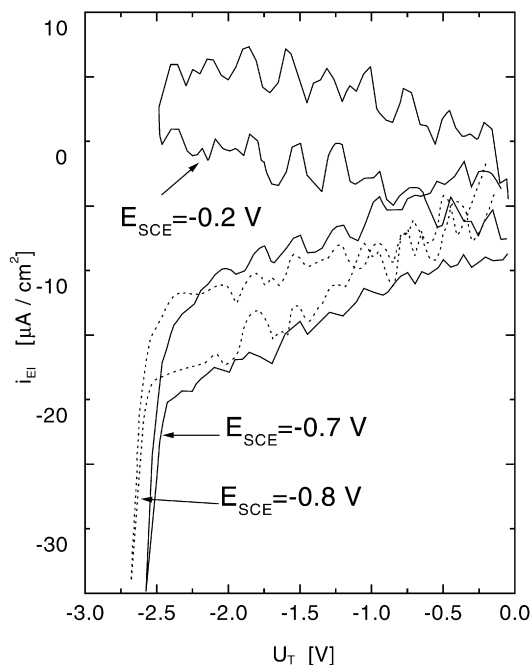
Fig. 11 Electrolyte current versus tunnel voltage at fixed electrode potentials of $E_{SCE} = -0.2$ V, $E_{SCE} = -0.7$ V, and $E_{SCE} = -0.8$ V. Tunnel current $I_T \approx$ mA cm^{-2} at $U_T = -2.6$ V
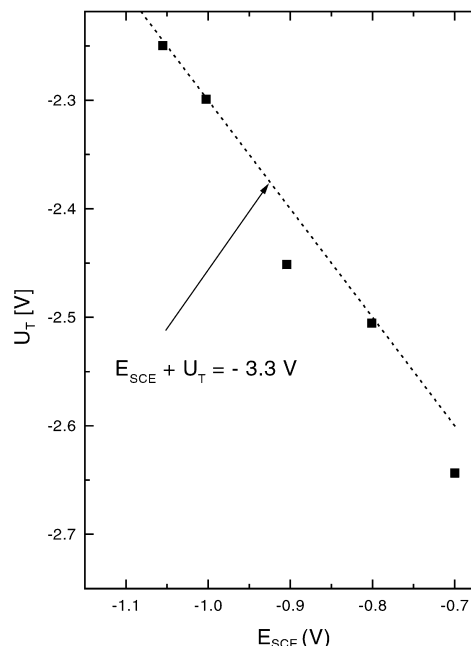

Fig. 12 Onset tunnel voltage of starting electron emission to the dry electron level PE (see Fig. 10) versus electrode potential. A *straight line* fulfilling $E_{SCE} + U_T = -3.3$ V is given for comparison

For comparison a straight line fulfilling

$$e_{SCE} + U_T = -3.3 \ eV \tag{3}$$

is given. This means that the threshold for photoemission of -3.4 V$_{SCE}$ is also valid for primary hot electron emission into the dry electron state by tunnel junctions. It also confirms that some of the tunneled electrons pass the top electrode elastically. One should note that the threshold value measured here in a 50%water/50% ethylene glycol electrolyte is within the range measured for pure aqueous electrolytes. For this reason we assume that the levels W and H are at about the same positions as in pure water. The measured current densities in the PE level are several hundred times higher than that of photoemission by continuous-wavelasers [12], if one considers the fact that a tunnel current of around 10 mA cm^{-2} causes a primary hot electron emission into the PE of 10 μA cm^{-2}. This means a transfer ratio, Q, of tunneled electrons from the Al electrode into the dry electron state of around 10^{-3}.

Hydrogen evolution by hot electrons

A fraction of the primary hot electrons reach ballistically the outer surface of the silver top electrode. The top electrode is connected simultaneously as a working electrode within an electrolyte. Figure 10 shows the levels of the electrons at the silver/electrolyte interface at an electrochemical potential of 0 V$_{SCE}$. For an applied electrochemical potential of -0.64 V$_{SCE}$ the H$_2$O/H$_2$
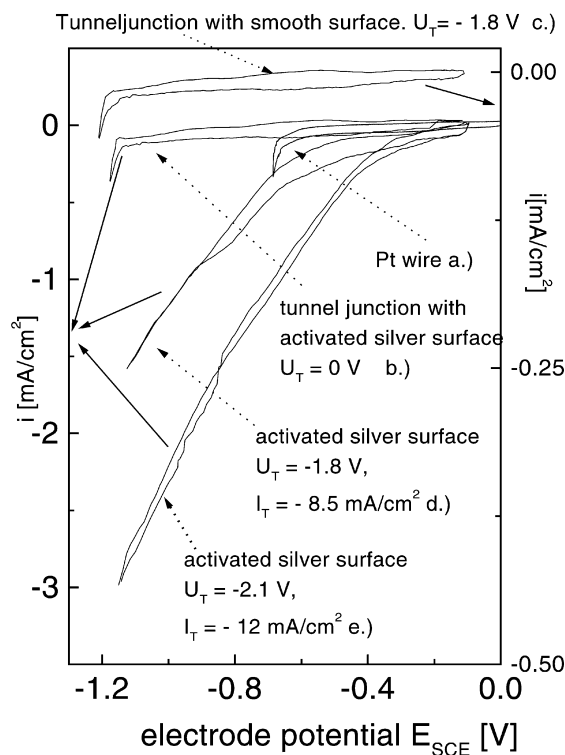

Fig. 13 Cyclovoltammograms of Pt wire and tunnel junctions in 0.9 M sodium acetate buffer (50% water, 50% ethylene glycol). *a* Pt wire, *b* activated top electrode $U_T = 0.0$ V, *c* unactivated top electrode $U_T = -1.8$ V, *d* activated top electrode $U_T = -1.8$ V, *e* activated top electrode $U_T = -2.1$ V

(Pt) level falls below the Fermi level of Pt and hydrogen evolution sets in (see the voltammogram in Fig. 13, scan a).

Owing to a very small exchange current for the HER on silver (in comparison to Pt), a just measurable small electrode current, I_{onset}, sets in only at a high overpotential (several 100 mV negative of the thermodynamic redox potential). Henceforth we call $\eta(I_{onset}$ at Ag electrode) $- \eta(I_{onset}$ at Pt electrode) the overpotential of the HER at a silver electrode. Given this definition, the overpotential of the HER at silver is negative.

The comparison with the voltammogram of the activated silver electrode of the tunnel junction at $U_T =$ 0 V (scan b) shows the onset of the HER only at about -1.2 V_{SCE}, corresponding to a cathodic overpotential of about -0.56 V_{SCE}. This behavior is nearly unchanged when a negative U_T is applied to the junction, provided this has not been "activated" or prepared rough intentionally, see scan c. However, when one prepares the junction on a rough CaF$_2$ substrate [39] or "activates" the silver electrode by a weak oxidation–reduction cycle ($E_{SCE} = +0.5$ V, $t = 0.2$ s) the HER sets in at more positive potential, see scan d. Moreover the onset potential of the HER is shifted by 300 mV to positive potentials, when the tunnel voltage is increased from -1.8 to -2.1 V (Fig. 13, scans d, e). This is clearly anodic with respect to the redox potential H$_2$O/H$_2$(Pt).

Detailed experiments under time resolution and at various values of U_T have demonstrated convincingly [43] that these reactions are not caused by ionic processes in the aluminium oxide film, nor by initial transition of the hot electrons into the levels of the electron in water given in Fig. 10.

A direct injection to state H, expected at an electrode potential of -0.98 V_{SCE} for $U_T = 0$ V can be safely excluded, because in all the voltammograms of silver ever recorded in aqueous electrolytes at pH≥7, where this emission should be well separated from the potential range of hydrogen evolution, the corresponding structure has never been observed (see, for instance, Ref. [76]).

In order to exclude pathways via the wet electron states, see Fig. 10, we performed analogous experiments at tunnel voltages U_T between 0 and -0.82 V, see Fig. 14. Experiments with voltammograms at more negative U_T are included in this figure.

Clearly the energies of the hot electrons at the low tunneling voltages are considerably below the wet electron states. Nevertheless about the same fraction, R, of the tunnel current continues as cathodic current into the electrolyte, as is evident by comparing the ratios given in Fig. 14. The vertical line is the H$_2$O/H$_2$ redox potential measured at a platinum electrode in the same electrolyte. With hot electrons near 2 eV, hydrogen evolution is possible at even more positive potentials (right-hand side of this line)! Note that the redox potential applies only to the thermodynamic equilibrium, in other words to reaction of electrons in the "Fermi sea". Hot electrons and their reactions are outside the equilibrium thermodynamic description.

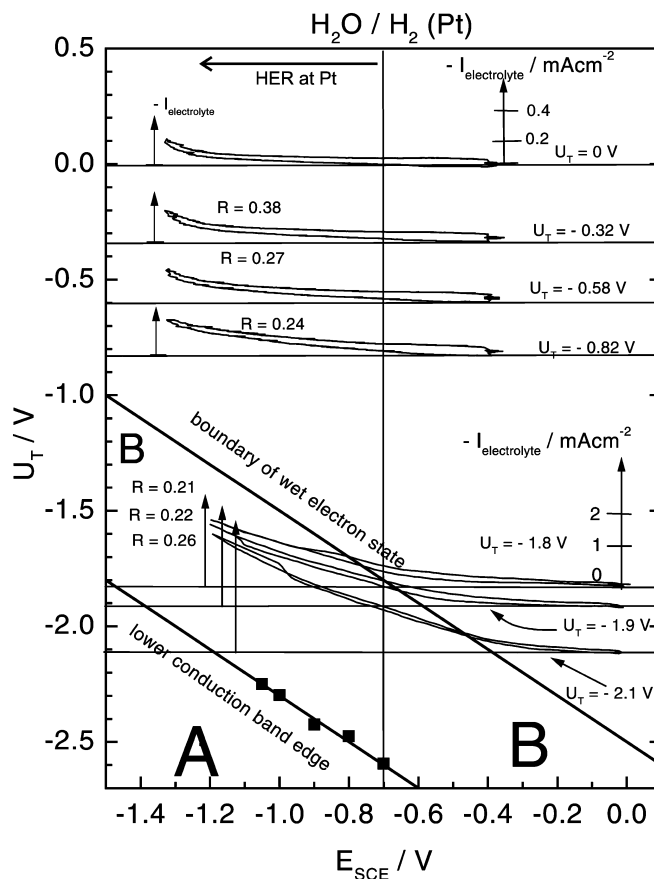The hot electrons overcome the kinetic hindrance of the HER; the hot electron reaction takes place in the

Fig. 14 *Region A*: range of tunneling voltage U_T and of electrochemical potential E_{SCE} in which electron emission into the electronic conduction band of the electrolyte is possible, see also Fig. 12. *Region B*: Range of U_T and E_{SCE} in which electron emission into the wet state (p-type state) of the electron in the electrolyte must be considered. Seven voltammograms [cathodic current ($-I_{electrolyte}$) as a function of E_{SCE} at different values of U_T) are displayed. The base lines ($I_{electrolyte} = 0$) of these are positioned at the proper values of U_T. R is the ratio of $I_{electrolyte}$ induced by the tunnel current I_T at the most negative values of E_{SCE}. The vertical line H$_2$O/H$_2$(Pt) is the onset potential of the hydrogen evolution reaction for a Pt electrode in the same electrolyte, see Fig. 13

electrochemical potential range between the potentials of the HER at platinum at about -0.74 V_{SCE} and at silver at about -1.2 V_{SCE}. Weak reactions are observed even at $E_{SCE} > -0.74$ V.

Hydrogen oxidation at silver surfaces

Cathodic potential pulses from -1.0 V_{SCE} to -2.0 V_{SCE} were applied to an epitaxial Ag(111) film in neutral 0.1 M KClO$_4$ aqueous electrolyte for 0.4 s, see Fig. 15b. During this time a faradaic cathodic charge, Q^-, of 4 mC cm^{-2} due to hydrogen evolution was accumulated, which corresponds to several monolayers (the charge corresponding to one electron per Ag surface atom of Ag(111) is 222 μC cm^{-2}). The integral of the anodic transient after switching back to -1.0 V_{SCE} is just the charge Q^+ involved in changing the voltage of the

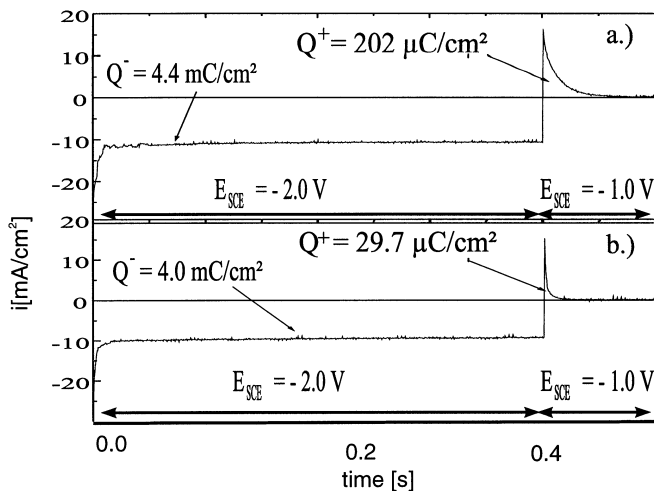**Fig. 15** Current transients on **a** activated Ag(111) and **b** smooth Ag(111) surfaces in 0.1 M KClO₄ after potential pulses from $E_{SCE} = -1.0$ V to $E_{SCE} = -2.0$ V and back from $E_{SCE} = -2.0$ V to $E_{SCE} = -1.0$ V

Fig. 16 Tunnel current at $E_{SCE} = -0.9$ V directly after the end ($t = 0$ s) of a cathodic pulse from -1.5 V_{SCE} to -0.9 V_{SCE} of 100 ms duration. The tunnel voltage is set from "accelerating" ($+0.3$ V) to "retarding" (-0.4 V). The time axis is scaled logarithmically. The electrolyte is aqueous 0.1 M KClO₄

electrochemical double-layer capacity; however, if the surface and the double-layer capacity of this Ag(111) film is increased by about 10% (by a short anodic pulse, leading to silver oxidation and reduction), the charge in the anodic transient corresponds to about 0.7 monolayers on top of the charge to account for the reordering of the double layer. This charge has been assigned to the reoxidation of a layer of atomically adsorbed hydrogen [77]. Also this reaction is related to hot electron chemistry, as demonstrated with a tunnel junction [56].

If an electrode with adsorbed hydrogen atoms is set by a potential step to an electrochemical potential of, for instance, -0.9 V_{SCE}, that is 0.3 V above the onset of hydrogen evolution, one may expect the injection of hot electrons with an energy of up to 0.3 eV above the Fermi level of the silver electrode. If these electrons from the reoxidation of adsorbed hydrogen tunnel into the Al electrode, one may use the junction as a retarding field energy spectrometer.

The variation of the tunnel voltage U_T in steps from "accelerating" at 0.3 V to "retarding" at -0.4 V is shown in Fig. 16. The transients in the tunnel current I_T after switching the electrode potential back to -0.9 V_{SCE} are obvious. At $U_T = -0.2$ V the transient is not yet fully suppressed, demonstrating that we do not observe a thermal effect. The constant tunnel current induced by the application of U_T is seen at about 0.1 s after the end of the anodic transients. Again we need a roughened silver top electrode of the tunnel junction to observe the anodic tunnel pulses. This and the previously mentioned results call for an explanation of the role of roughness in hot electron transfer.

The contribution of secondary hot electrons below 1 eV is possible, because as demonstrated in Fig. 14, primary hot electrons below 1 eV also induce HER. However the relative contribution of primary and secondary electrons to HER cannot be predicted, because
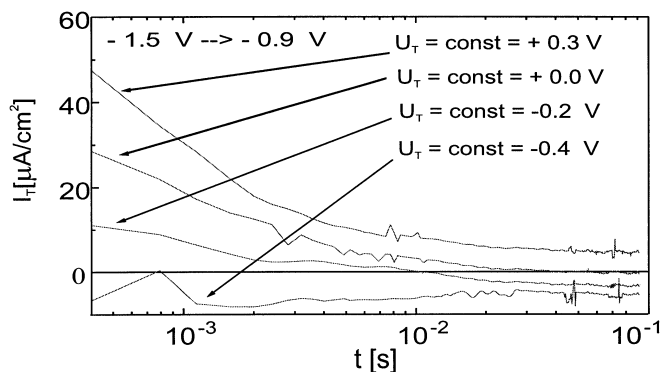
primary and secondary electrons reaching the outside silver interface will have different angular distributions. In the "dephasing model", see later, the tunnel current is partly controlled by the dephasing of the primary electrons at the outside silver interface. The incidence rate of secondary hot electrons at the interface will scale with the tunnel current, but will also depend on the energy of the secondary electrons.

## Model of the role of roughness in hot electron transfer

Normal hydrogen evolution

By X-ray scattering at the interface of Ag(111) with an aqueous NaF electrolyte, Toney et al. [79] observed a layered structure of the oxygen distribution. At a potential of $E_{SCE} = -0.9$ V the maximum of the distribution was about 0.35 nm in front of the top (111) plane of the Ag ion cores. This distance changed to about 0.28 nm at the potential of $E_{SCE} = -0.15$ V. This difference was assigned to a reorientation of the water molecules in the inner Helmholtz plane, the oxygen end situated nearer to the interface at anodic potentials and the hydrogen end nearer to the interface at cathodic potentials.

Theories of the hydrogen evolution in low-pH electrolytes involve potential-dependent reorientations of the water molecules in the first layer and hydronium ions in the second layer (the outer Helmholtz layer) and proton transfer (e.g. Ref. [79] and references therein). Hydrogen evolution in neutral-to-basic electrolytes probably involves tunneling of electrons from the metal into water molecules H_2O_{iHp} in the inner Helmholtz plane. This electron transfer can split the molecule and drive the Volmer reaction (for more details see Ref. [77]).

$$H_2O_{iHp} + e^- \rightarrow OH^-_{iHp} + H_{ad}. \qquad (4)$$
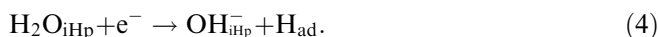
The further charge transport probably involves the steps of proton transfer between the inner and the outer Helmholtz plane

$$OH^-_{iHP} + H_2O_{aHp} \rightarrow H_2O_{iHp} + OH^-_{aHp} \qquad (5)$$
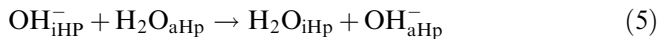
and a modified Grotthus mechanism in the bulk electrolyte by proton transfer

$$OH^- + H_2O \rightarrow H_2O + OH^-. \qquad (6)$$
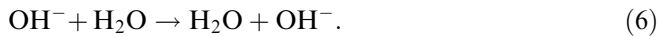
Hydrogen evolution by hot electrons

The hydrogen evolution by hot electrons takes place at a lower cathodic potential than the usual hydrogen evolution, which involves only "cold electrons" of energy at and below the Fermi surface. In this case the ordering of the water molecules is probably not the same as at the onset of the usual "cold electron hydrogen evolution". The basis of our model of hydrogen evolution from H_2O by hot electrons is as follows. The tunneling probability grows quasiexponentially with the extension of the tail of the electronic wavefunctions into the double layer. At a certain threshold of the "penetration depth" the Volmer reaction starts. The penetration depth is a function of the electronic energy and momentum parallel to the surface and the applied electrochemical potential. The energy momentum relation of the bulk electrons (which are involved in the observed transport processes) is given by the bulk band structure. The only information on the electron in the electrolyte we use is the energetic position PE of the lower band of the electronic conduction band, the so-called "dry electron". The penetration length of the bulk electrons of energy E into an electrolyte is calculated analogously to the penetration of free metal electrons into a vacuum, with replacement of E_{vacuum} by PE. The electron wavefunction outside the last layer of the cores of the silver surface atoms is assumed to be free-electron-like (we neglect a possible increase of the mass because of interaction with the inner Helmholtz layer), with a relation between the wave vector, k, and the energy, E, given by

$$\frac{k^2}{2m} = E - PE, \quad k = ||. \qquad (7)$$

The wavevector $k = (k_x, k_y, k_z)$ has the normal component k_z, which is imaginary when

$E < PE$. *In this case, we set* $k_z = i\kappa$. $\qquad (8)$

In Eq. (7) E is the energy of the bulk electron and $k_{||} = (k_x, k_y)$ is the tangential component of the bulk part of the $\mathbf{k}$ vector of the electronic wavefunctions, because of the continuity of the wavefunction across the metal/electrolyte interface. The decay length, L, of the wavefunction of electrons within the electrolyte is $\frac{1}{\kappa}$.

The difference PE – E_F varies with the electrochemical potential E_{SCE} according to [47, 75]

$$PE - E_F = 3.3eV + e_{SCE}. \qquad (9)$$

At $k_{||} = 0$, L diverges when E reaches PE, because now the electron can enter the bulk electrolyte, as observed by photoemission into the electrolyte (hence the abbreviation PE [47, 75]).

The role of roughness

Our general argument on the role of surface roughness is derived from the fact that there are gaps in the surface-projected bulk electron density of states for the silver (111) and (100) surface [80]: see Figs. 17, 18, 19. That means that for the (111) oriented electrodes there are only propagating bulk hot electrons at $E - E_F > 2$ eV with components k_x and k_y of k above minimum values. Consequently hot electrons propagating normal to the surface do not exist. Related effects have been clearly observed in secondary-electron-emission and absorbed-current spectra of Ag(111), (100) and (110) [82]. The hot electrons arrive at (111) surfaces only at oblique incidence and therefore have a relative small decay length, L. But when the surface is not perfect, these electrons may be scattered by atomic scale roughness into states with larger L. Larger L means that the tunneling probability to the lowest unoccupied molecular orbital of adsorbed molecules, atoms, and ions grows.

We try to quantify this for the Ag(111) surface. For hot electrons in silver films of (111) orientation there is, caused by a gap in the surface-projected density of bulk electronic states [80] Fig. 17, a minimum value

$$k_m(E_{hot}) \text{ of } k_{||} = \left(k_x^2 + k_y^2 \right)^{\frac{1}{2}}$$

as function of

$$E_{hot} = E - E_F = -eU_T, \qquad (10)$$
see Figs. 18 and 19.

Given these conditions, one easily derives

$$L \leq L_{max,\, smooth} = \frac{1}{\sqrt{\left| \frac{2m(-e1U_T - 3.3eV - eE_{SCE})}{\hbar^2} - k_m^2(E_{hot}) \right|}}$$
$$(11)$$

$L_{max,smooth}$ is shown as a function of E_{SCE} for $e \cdot U_T = 0$, –1.8, and –2.1 eV, and for $U_T = -1.0$ and –0.5 V in Fig. 21.

Our hypothesis is the elastic scattering of hot electrons by atomic scale surface roughness to laterally (parallel to the surface) and perpendicularly (versus the interior of the crystal) damped states with the real part of the parallel wavevector $k_{||} < k_m(E_{hot})$, so-called virtual states in the gap of the projected density of states in Fig. 18. These virtual states may comprise the Shockley surface states which are at the clean surface at $k_{||} = 0$ below the Fermi energy, but which may be pushed upward by the adsorbates. They are orthogonal to the bulk states at a perfectly smooth low-index surface, but
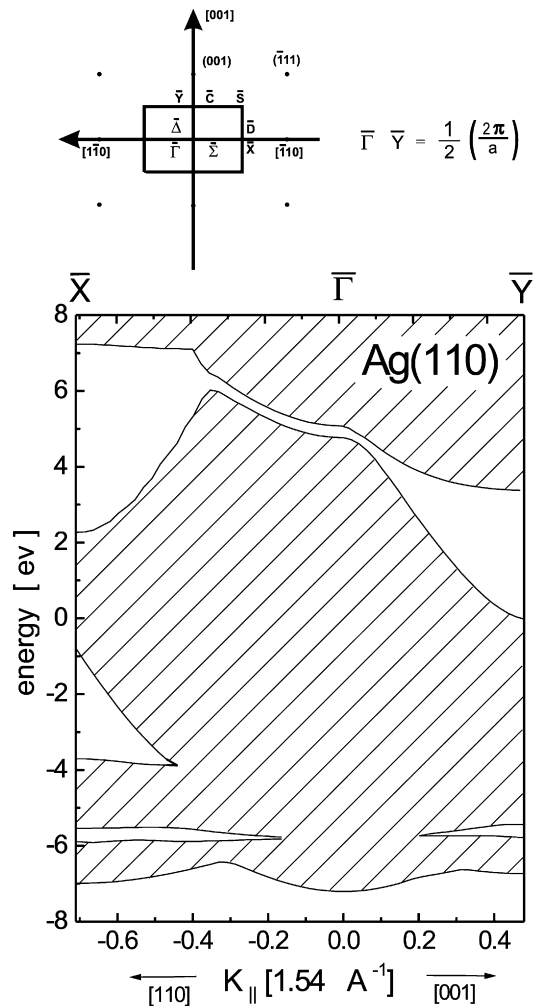
Fig. 17 Surface projected bulk electron density of states (*shaded*) of Ag(110) in $\bar{X} - \bar{\Gamma} - \bar{Y}$ direction. The $k_\parallel$ directions are indicated in the surface Brillouin zone above. The energy E is given relative to E_F. Positive energy values correspond to the energy E_{hot} of hot electrons, see Eq. (10). Data from a self-consistent relativistic density functional calculation [81]

Fig. 18 Like Fig. 17, but for Ag(111) and $\bar{Gamma} - \mathbf{M}$ direction

atomic scale roughness (e.g. fuzzy steps) may allow conversion of hot electrons into these virtual-state electrons. The scattering into virtual states will increase the right-hand side of Eq. (12), which will reach its maximum for $k_\parallel = 0$.

The limit is given by

$$L \leq L_{\text{max,rough}} = \frac{1}{\sqrt{\dfrac{2m \cdot (|-eU_T - 3.3\text{eV} - e \cdot E_{SCE}|)}{\hbar^2}}}, \qquad (12)$$

see also Fig. 20 for $e \cdot U_T$ equal to 0, –0.82, –1.8, and –2.1 V. Note that $L_{\text{max,rough}}$ depends only on $(U_T + E_{SCE})$.

The experimental onset of the hydrogen evolution at an activated surface by hot electrons at $U_T = -1.8$ V is at about $E_{SCE} = -0.6$ V (see Fig. 13), where $L_{\text{max,rough}} = 0.195$ nm, according to Fig. 20 (point at –0.6 V_{SCE}). We obtain the same value of $L_{\text{max,rough}}$ for $U_T = -2.1$ V at $E_{SCE} = -0.3$ V (see right point in Fig. 20), which corresponds with the observed onset of
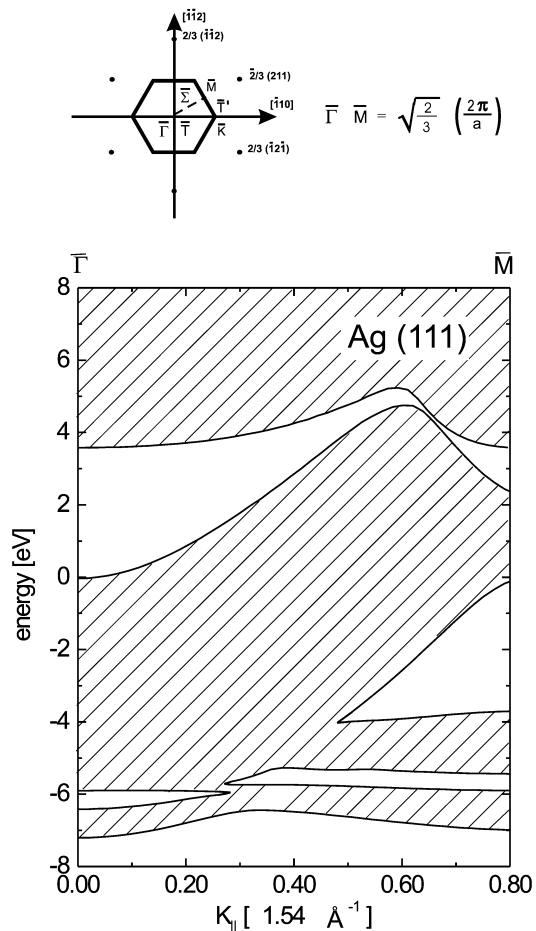
hydrogen evolution at $U_T = -2.1$ V (see Fig. 13). Equation (12), valid for the smooth surface, gives $L_{\text{max,smooth}} = 0.144$ nm at $U_T = -1.8$ V and $E_{SCE} = -0.6$ V (see Fig. 20).

The curve for a smooth surface at $U_T = -0.82$ eV is not included in Fig. 20. It is only about 0.05 Å above the decay length, L, at $U_T = 0$ V, the difference between curves 4 and 5 in Fig. 21.

The role of the roughness can be understood, if we assume that $L \approx 0.195$ nm allows the hot electron to reach and dissociate the water molecules in the inner Helmholtz layer (with the structure of the double layer at $E_{SCE} \approx -0.5$ V), whereas the lower value of $L_{\text{max,smooth}} = 0.144$ nm is not sufficient for this. For $U_T = 0$ V the "normal, cold electron hydrogen evolution" is observed at $E_{SCE} = -1.2$ V, see Fig. 13. At this potential both the calculated values of $L_{\text{max,rough}}$ and $L_{\text{max,smooth}}$ are about 0.124 nm (see Fig. 20, left point). We can understand why this relatively low value of L allows hydrogen evolution, if we assume that at this rather cathodic potential the double layer is reoriented and now allows the transfer of the "cold" electron into the inner Helmholtz layer with subsequent dissociation of water, as discussed already.

The modelling of the metal/electrolyte interface by Pecina and Schmickler [79] showed a reorientation of the
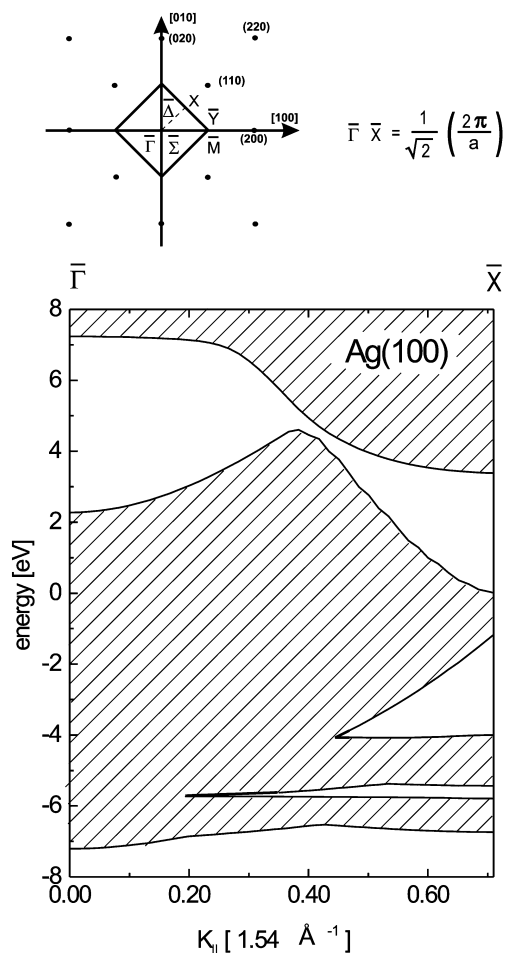
Fig. 19 Like Fig. 17, but for Ag(100) in $\bar{\Gamma} - \bar{X}$ direction

Fig. 20 Maximum decay length, L, of the electron wavefunction within the electrolyte as a function of the electrochemical potential, E_{SCE}, for smooth and rough silver(111) electrodes according to Eq. (12) for the indicated tunnel voltages U_T. The *points* on the curves for rough surfaces, parameter U_T, give the potentials of the onset of the HER, taken from Figs. 13 and 14 for parameter U_T

water O–H groups in the inner Helmholtz layer towards the surface by the strong electric fields in the double layer at a cathodic potential which may allow the necessary electron transfer even at smaller values of L.

The points in Fig. 20 may reflect this potential-dependent reorientation. The approximate agreement of $L_{max,rough}$ and $L_{max,smooth}$ at $E = E_F$ may explain why roughness of the silver electrode reduces the overpotential of the normal hydrogen evolution only very little. Our model would yield a less cathodic onset of hydrogen evolution by hot electrons at smooth silver electrodes, which is not indicated in Fig. 13. However there may be some experimental indication for this process in Ref. [74]. To the best of our knowledge, this is the first model of hydrogen evolution which not only involves orientational effects in the double layer, but also a potential-dependent penetration of the metal electrons into the inner Helmholtz layer.

Conjectures on activation

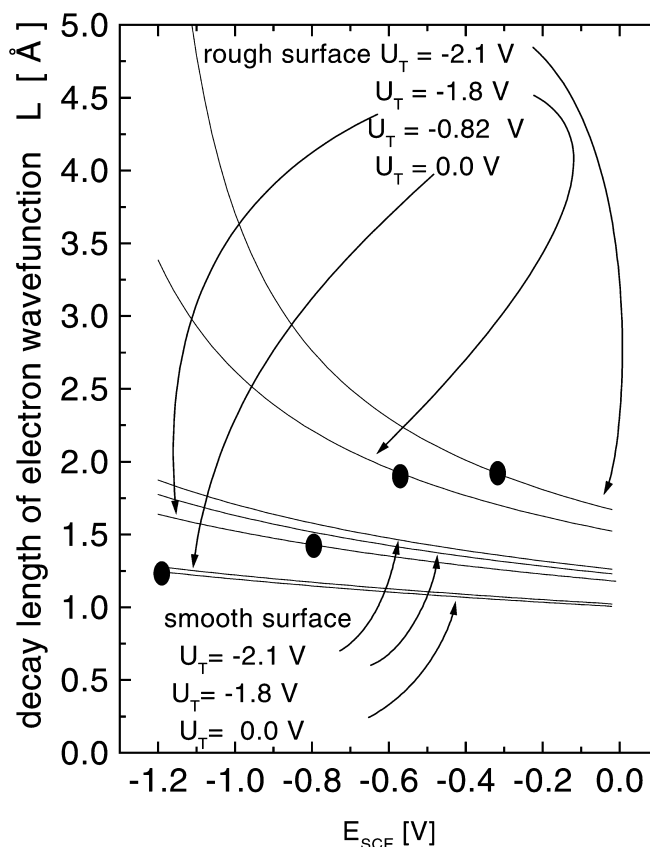Our hypothesis is based on the elastic scattering of hot electrons by atomic scale roughness of Ag(111) surfaces.

This implies that two conditions must be fulfilled in order to observe the HER by hot electrons:

1. A sufficiently high surface concentration of special atomic scale roughness sites at a surface of prevailing (111) orientation.
2. Sufficient overlap of bulk and virtual surface states at and near these special sites of atomic scale roughness to allow hot electron transfer.

The hydrogen evolution by hot electrons has been observed using tunnel junctions undercoated with a rough CaF_2 film of 100-nm thickness. By measuring the electrochemical capacity of these samples and a silver (111) single crystal one may define a roughness factor as the ratio of the capacities of the rough and smooth sample, both capacities normalized with respect to the apparent surface area. The roughness factor obtained in this way ranged between 1.2 and 1.7. The layer of adsorbed hydrogen on an epitaxial Ag(111) film was observed after an increase of the surface by 10% by a fast oxidation–reduction cycle. Surprisingly, the activation of the tunnel junctions on glass substrates needed only the oxidation and subsequent reduction of half a monolayer of silver. The related increase in the surface area is
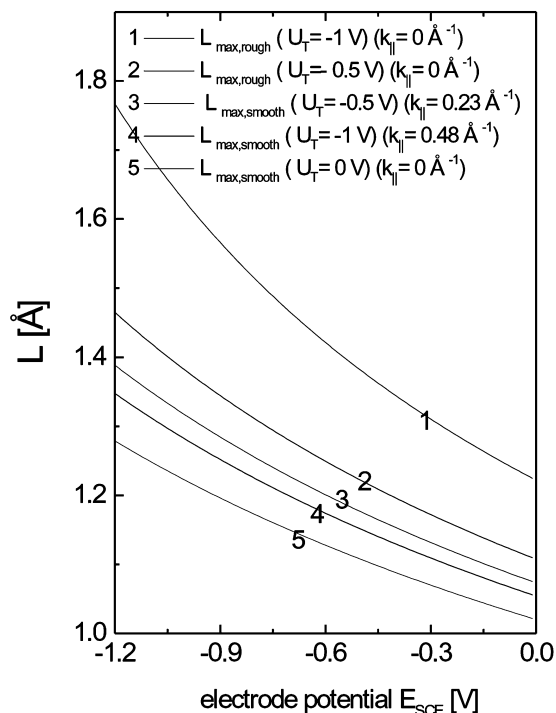
Fig. 21 Maximum decay length, L, (calculated in the same way as in Fig. 20 for small tunnel voltages) of the electron wavefunction within the electrolyte as a function of the electrochemical potential, E_{SCE}, for smooth and rough silver (111) electrodes according to Eq. (12) for the indicated tunnel voltages U_T

Fig. 22 Voltammograms of an Ag(111) crystal, on which various numbers of monolayers of Pt have been evaporated, in 50 mM $KClO_4$ aqueous electrolyte. Potential scan speed 50 mV s^{-1}. Taken from Ref. [76]

negligible. Therefore we think that the activation is needed to fulfill condition 2. Maybe the activation reflects the cleaning of active sites from unknown adsorbates which prevent efficient electron transfer. However, activation was not necessary on the CaF_2 roughened samples to which these unknown adsorbates would probably stick as well. Therefore we envision the activation as the transformation of already existing linear monoatomic steps into static fuzzy steps with a high density of kink sites, by the partial dissolution of terraces, starting at steps and the subsequent redeposition of the material on the terraces, from which it migrates to the steps but does not diffuse along the steps. On the other hand, a silver film contouring the rough CaF_2 substrate would have many stable kink sites, and therefore would not need activation. Checking these conjectures will need careful scanning tunneling microscopy of the nonactivated and of the activated surfaces. Our model reflects the experimental observations only very approximately. This is not surprising given the very simple theoretical assumptions made for a complicated problem. Since we see no other concept yet to explain the observed influence of the activation we resort to an experimental approach to check the concept of roughness-controlled penetration depths, L. Experiments on Ag(111) electrodes with better controlled roughness are under way [76]. We tentatively explain the role of roughness in the observed reoxidation of atomic hydrogen in an analogous way. Electrons in the virtual
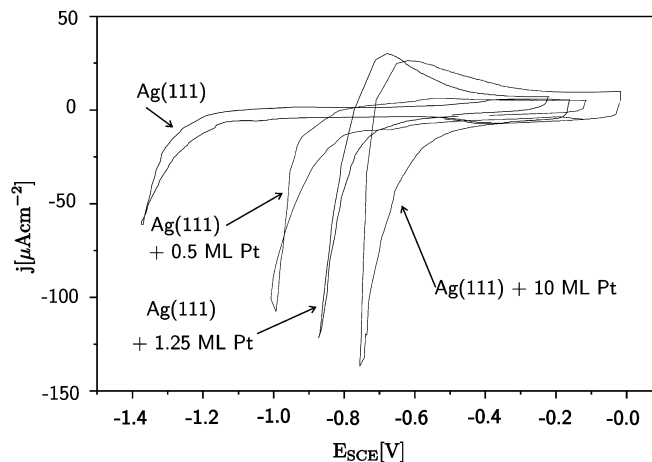
bound states, which extend further out, can only hybridize with the bulk states in the presence of special roughness sites where the electron from adsorbed hydrogen can be released to Ag(111) bulk states. This process can be considered as the time-reversed reduction process discussed earlier. It should be noted that the critical penetration depths, L, necessary for the Volmer reaction and the oxidation of adsorbed atomic hydrogen are probably different. Without or with little activation, the electron-transfer rate to the bulk will be low and the Tafel reaction

$$H_{ad} + H_{ad} \rightarrow H_2 \tag{13}$$

will have the higher reaction rate and will take over.

Redox reactions at platinum clusters
on Al/AlO$_x$/Ag junctions

The overpotential of the hydrogen evolution at silver single-crystal electrodes in 50 mM $KClO_4$ electrolyte is reduced by a coverage with evaporated platinum clusters, see Fig. 22 [76]. Our aim was to study this system with MIMs; however, the heat radiation from the thermal evaporation sources destroyed the function of the MIMs. Therefore we chose stabilised platinum clusters. The platinum clusters were produced by reduction of $PtCl_2$ in an aqueous tetrahydrofuran electrolyte. The clusters had a mean diameter of about 1.5 nm and were stabilized against aggregation (sintering) by a surfactant layer of betain [3-(dimethyldodecylammino) propane sulfonate] [83].

A surface layer of betain on a platinum electrode partly inhibits the hydrogen underpotential deposition, but does not change the onset of hydrogen evolution, it only slows down the mass transport between liquid electrolyte and the electrode [84]. These phenomena have been investigated in detail for proton migration

and water diffusion in polyaniline films on palladium and gold electrodes [85]. If the reduction of water took place at the interface between the surfactant and the electrolyte, involving electron transfer through the surfactant, the overpotentials of Au with respect to Pd should disappear, contrary to the observation [85].

A drop of an aqueous solution of the clusters was put on the MIM and dried. The surface coverage of the clusters could be controlled only approximately. The clusters remain fixed to the silver surface when the MIM is inserted into the 0.05 M $KClO_4$ electrolyte of a 1:1 mixture of water and ethylene glycol. Also in this case a decrease of the overpotential of the HER on silver is observed, see the voltammograms in Fig. 23 [43]. The oxidation and reduction of ethylene glycol does not take place in the electrode potential range of the voltammograms in Fig. 23 [87]. We conclude that the hydrogen evolution takes place at the surface of the Pt clusters by reduction of water.

In the top panel of Fig. 24 the electrode current, i_{El}, is plotted versus the electrode potential, E_{SCE}, during a cathodic sweep with -50 mV s^{-1} from A to B into the hydrogen evolution range, an anodic sweep back from -1.1 V (point B) to $E_{SCE} = 0.5$ V (point D) with 50 mV/s^{-1}. The positive electrode current starting at point C is caused by the oxidation of the species obtained by the water reduction (see also Fig. 25). A third linear cathodic sweep from D to B follows; up to point E there is still oxidation. These voltammograms do not depend on the applied tunnel voltages, U_T. The middle panel of the figure shows the tunnel currents, i_T, measured simultaneously with the voltammograms for two values of U_T. At $U_T = 0$ V, there is no tunnel current during the first cathodic sweep from A to B. However, for the next two sweeps there is a positive tunnel current when oxidation is going on, from C to D and from D to E. Then, U_T was set to 0.1 V, leading to a constant tunnel current of

about 3 µA cm^{-2} during the scan from A to B. During oxidation in the next two sweeps from C to D and from D to E, i_T is larger than during the first scan from A to B. In the bottom panel of the figure the extra electron charge, q_T, reaching the aluminium electrode during the three sweeps,

$$q_T = \int_0^t (i_T(t) - i_T(A))dt,$$

is plotted during the three sweeps. At $U_T = 0.1$ V, the extra charge at the end of the three sweeps is more than double its value at $U_T = 0$ V.

Figure 25 [87] corresponds to Fig. 24, top and middle panels, at $U_T = 0$ V. It clearly demonstrates that the extra tunnel current in the anodic sweep is caused by the reduction of water in the previous cathodic sweep. In summary, there is a significant difference between reduction and oxidation; only in oxidation is a contribution to the tunnel current observed. In Fig. 24 the anodic end of all the sweeps was at $E_{SCE} = -0.5$ V; in Fig. 26 [87] this is at $E_{SCE} = -0.2$ V and also negative tunnel voltages are applied. Here the MIM acts as a retarding field spectrometer, measuring the maximal energy of the electrons injected during oxidation about 0.2 eV above the Fermi level of silver.

The difference in the injection of electrons from states just below the Fermi level of Ag into the electrolyte by reduction of water and the injection of electrons some 100 meV above the Fermi level of silver by oxidation of
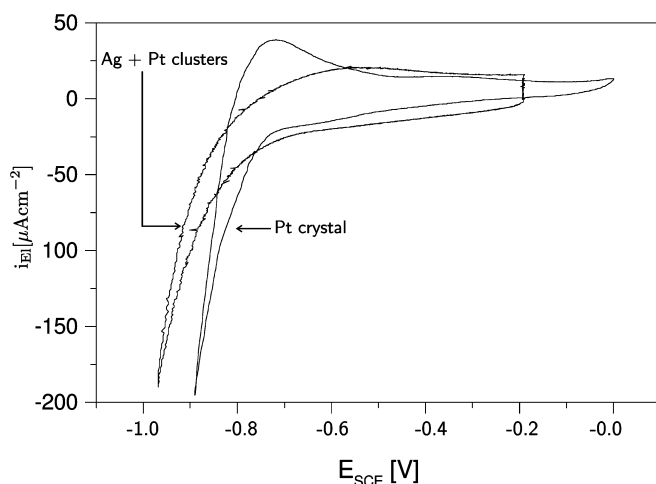

Fig. 23 Voltammogram of a half sphere of a Pt crystal, grown according to Clavillier [86], and of Pt clusters (see text) on the Ag electrode of an Al–AlO$_x$–Ag junction, both in 0.05 M $KClO_4$ water–ethylene glycol (1:1) electrolyte
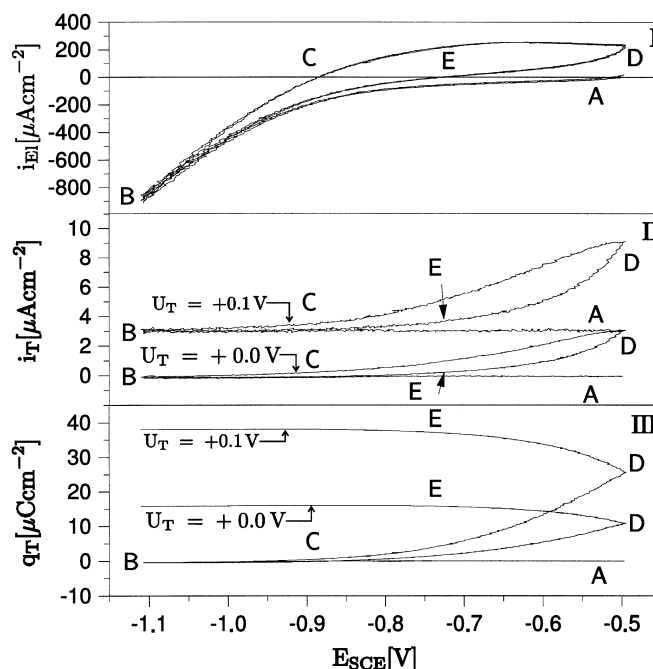

Fig. 24 MIM junction with the silver electrode covered by Pt clusters in the same electrolyte as in Fig. 23. *Top*: voltammogram during three sweeps with $\left|\frac{dE}{dt}\right| = 50 \frac{mV}{s}$. *Middle*: simultaneously monitored tunneling current (positive when electrons flow from Ag to Al). *Bottom*: accumulated charge, see text. Taken from Ref. [43]
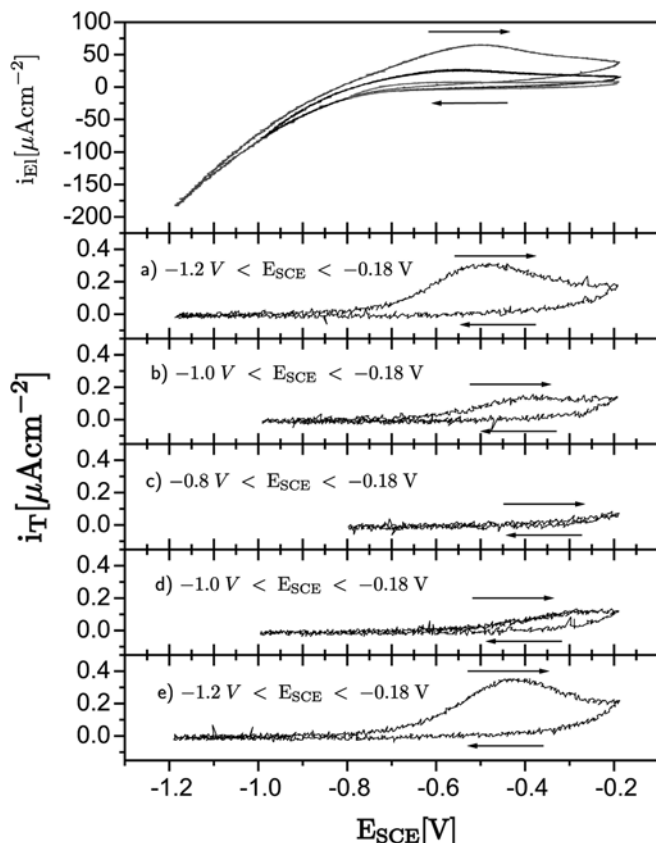
Fig. 25 MIM junction with the silver electrode covered by Pt clusters in 0.05 M LiClO$_4$ in water ethylene glycol (1:1) electrolyte. Tunnel currents during potential sweeps with different cathodic end potentials. Tunnel voltage $U_T = 0$ V. Taken from Ref. [87]

Fig. 26 Like Fig. 25, but with fixed cathodic end potential and indicated values of U_T. Negative U_T yield retarding conditions for the electron current from Ag to Al electrodes of the junction

hydrogen or OH is striking. The injection of electrons into the electrolyte may be considered as injection of holes into the silver metal. As explanations of the difference of the injected electron and hole energies (of the order of 100 meV or near zero, respectively) we can exclude firstly the difference in the mean free path of holes and electrons in the sense that holes do not reach the Ag–AlO$_x$ interface, but electrons do. However, at these low energies compared to the Fermi energy, the mean free path of electrons and holes at the same energy is equal [44]. Secondly we can exclude as an explanation a smaller tunneling probability from Ag to Al of electrons with a small energy, ΔE, below E_F compared to electrons with energy ΔE above E_F. The ratios calculated for a barrier of 2-nm thickness and offsets of the AlO$_x$ conduction band of 3.9 eV at the silver side and 2.5 eV at the Al side is at most 2.5; it cannot explain the missing change of the tunnel current during the reduction of water. There might exist a small activation barrier for the oxidation process which is missing in the reduction process. One of the authors (A.O.) also considered an explanation based on a unidirectional Coulomb barrier. The important prerequisite is that the betain layer survives between the platinum colloid and the silver top electrode of the MIM and is not squeezed out.
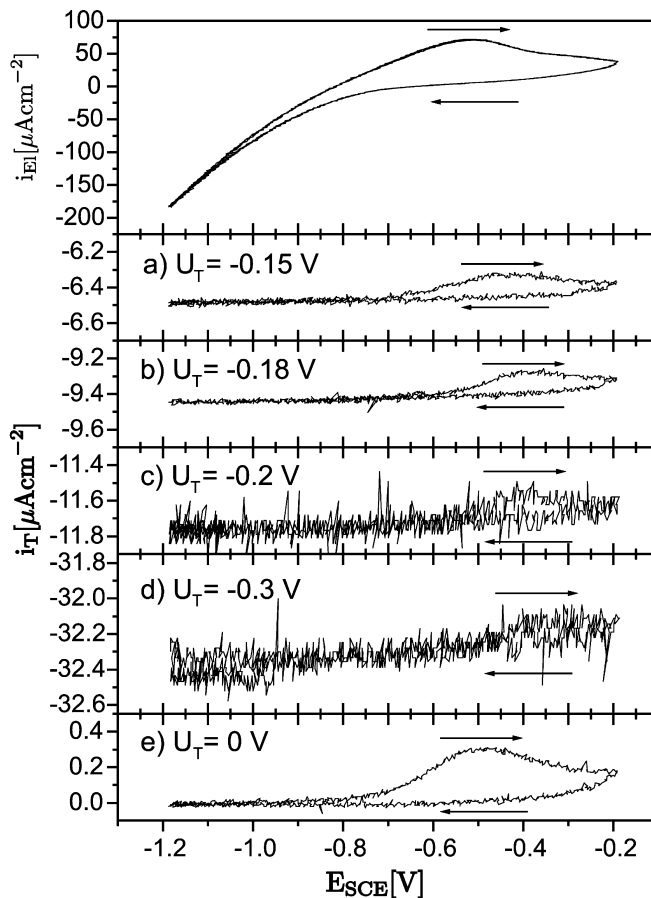
This point remains as yet open, but is not unlikely. The model of a Coulomb barrier was used in explaining the manipulation of alkane-coated gold nanocrystals using scanning tunneling microscopy [88].

Coulomb barriers occur when very small capacities are charged. Putting an electronic charge e on a capacity C requires a voltage U of $\frac{e}{C}$. For $C = 10^{-18}$ F, $U = 160$ mV. The capacity of a solid metal sphere of radius r in a medium of dielectric constant ϵ is given by $4\pi\epsilon_0\epsilon r$.

For a sphere of 0.75-nm radius and the static dielectric constant of water $\epsilon = 80$ one obtains $C = 6.67\times10^{-18}$ F and $U_{coulomb} = 23.9$ mV.

If one assumes as the dielectric a tenside layer with intercalated water, hindered in full rotation, one may assume $\epsilon = 10$, which yields $U_{coulomb} = 191$ mV.

The problem with this hypothetical explanation is that the Coulomb blockade and Coulomb staircase in single-electron tunneling through clusters has always been observed in both transport directions, for instance, by putting cobalt nanoparticles of 3–6-nm diameter on an Au(111) surface covered with a thin 1–2-nm-thick Al$_2$O$_3$ film and taking the tunnel I–V curve with the tip of a scanning tunneling microscope positioned over the particle [89]. Formally it seems possible to replace the

capacity between the tip and the cluster by the capacity of the Helmholtz layer around the Pt clusters, which one may estimate easily as being in the range of 10^{-18} F. Also the criterion for the tunneling resistance per cluster exceeding $\frac{\hbar}{e^2} = 4.1; k\Omega$ is easily met. It remains a problem to explain the unidirectionality.

Dependence of the internal tunnel current on the surface conditions of the top electrode

Usually, electron tunneling experiments between two stratified conductive films involve film thicknesses much larger than the mean free path of the tunneling electrons. In this case, the tunnel current density, I_T, is determined by the properties of the tunneling barrier and the electronic density of states within the bulk of the two films [90, 92]. Outer surfaces of the two films are not involved. Changes have to be expected, when at least one film thickness is decreased and reaches the order of the mean free path of the hot tunneling carriers. Related to this is the so-called ballistic electron emission spectroscopy [92, 93], where electrons tunneling between a thin metal film on a semiconductor and the tip of a scanning tunneling microscope yield information on the buried interface between the metal and the semiconductor.

In the case of MIM junctions we have two rather clear-cut schemes to influence the tunnel current at constant tunnel voltage by changing conditions at the noble metal interface with an electrolyte or with UHV:

- Firstly, by allowing for faradaic reactions driven by hot carriers at the electrolyte interface or by emission into the electrolyte or the vacuum.
- Secondly, by modulating the dephasing of tunneling states, for instance, at UHV interfaces by adsorption, without an emission current into the vacuum.

There are examples for dephasing without faradaic reactions both at metal/UHV and metal/electrolyte interfaces. We describe these results first in the next subsection and give a model for dephasing at the surface in the subsequent subsection. As yet we have not found a faradaic reaction without a strong dephasing contribution.

Controlling the internal tunnel current without faradaic reactions

The change of tunnel current at constant tunnel voltage by adsorption of potassium from –0.17 to –0.55 mA and by adsorption of oxygen from –0.02 to –0.01 mA was already reported in Ref. [50]. These strong changes were not understood at that time. They are clearly not caused by faradaic effects. To elucidate the origin of this effect we performed further experiments with $Al/AlO_x/Ag$ systems in UHV [94]. We chose anodic oxide layers, because they show a very weak temperature dependence of the tunnel current from 290 to 45 K. When evaporating

a 2.6-nm silver film on top of a 20-nm-thick silver top electrode of an MIM junction at 45 K, the tunnel current at a constant tunnel voltage of, for example, $U_T = -1$ V, increases by a factor of 5.7. This current increase vanishes nearly completely when the MIM junction is heated up to room temperature again. This corresponds to the considerable increase of the electrical direct current resistance of a smooth silver film (thickness 26 nm) from 0.69 to 0.87 Ω by cold deposition of 3 nm of silver at 59 K [95]. This increase vanishes nearly completely by annealing to room temperature [95].

The increase of the direct current resistance is caused by diffuse scattering of the electrons at the Fermi level by the unordered structure of the cold-deposited silver. In analogy, the origin of the modification of the tunnel current is a dephasing process at the top electrode surface of the MIM junction by diffuse scattering by atomic scale roughness, see later.

The increase of the tunnel current, I_T, at constant tunnel voltage, U_T, by roughening on an atomic scale, given by the quotient

$$Q = \frac{I_T(\text{rough, } U_T)}{I_T(\text{smooth, } U_T)}$$

depends strongly on the tunnel voltage. We found $Q = 5.7$ for $U_T = -1.0$ V. An explanation of this effect is given later.

Kritzler [43] observed an analogous tunnel current increase due to surface roughening of an $Al/AlO_x/Ag$ junction in a 0.05 M $KClO_4$ water/ethylene glycol electrolyte. He used a small overpotential of 100 mV to bring submonolayer amounts of silver on the top electrode surface of an $Al/AlO_x/Ag$ junction (with initially flat surface). The potential was held at $E_{SCE} = 0.1$ V with tunnel voltage $U_T = $ constant $ = -0.5$ V. At $t = 0 s$ $AgClO_4$ was added. The resulting concentration was 0.3 mM of $AgClO_4$.

Figure 27 shows that the tunnel current increases drastically when the silver starts to adsorb on the flat top electrode surface. In the upper part of Fig. 27 the electrolyte current increase caused by the reduction of Ag^+ is shown; the middle part shows the integrated electrolyte current. After about 100 s just one monolayer of Ag was deposited on the surface of the tunnel junction. The lowest part of the figure shows the corresponding tunnel current. It rises within the first 3 s by about 60% although just 5% of a monolayer of Ag has been adsorbed.

At least in the case of cold deposition of silver on a MIM junction in UHV no faradaic reactions are involved.

Firstly we try to discuss the results by a ballistic model [94]. We assume a starting rate of J_0 electrons per unit area at the oxide/silver interface. This would correspond to the tunnel current of the given MIM junction with the silver film thickness increasing far beyond the mean free path of the starting electrons. For silver top electrodes of a thickness of the order of the mean free
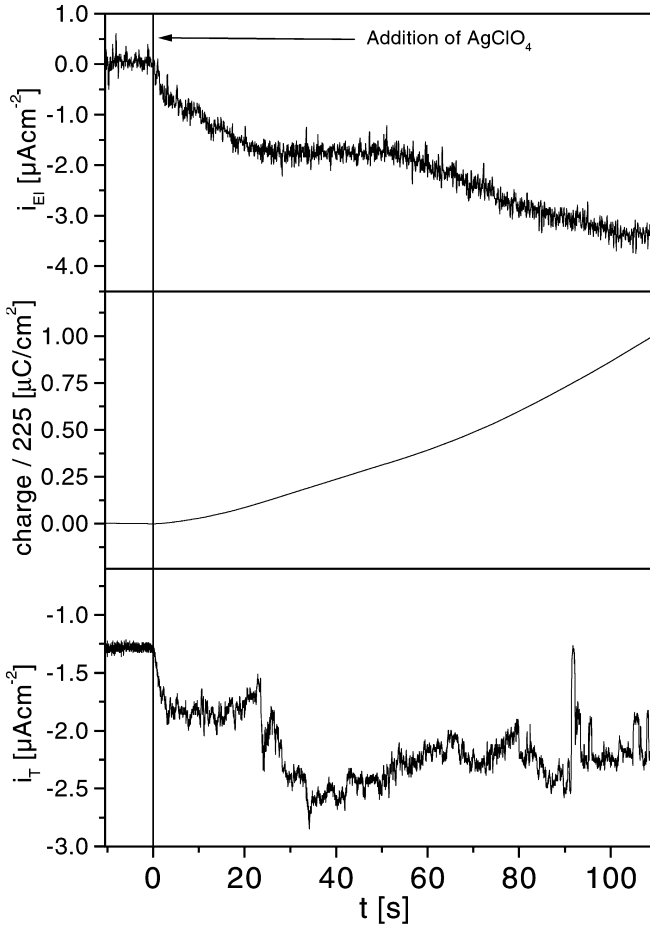
Fig. 27 Deposition of a monolayer of silver on the silver top electrode of an Al/AlO$_x$/Ag junction. *Top*: electrode current versus time at $E_{SCE} = +0.1$ V after injection of AgClO$_4$ resulting in a concentration of 0.3 mM AgClO$_4$. *Middle*: deposited amount of silver (obtained by integration of curve 1) *Bottom*: tunnel current at constant tunnel voltage of $U_T = -0.5$ V. Taken from Ref. [43]

path, the ballistic elastic current density at the silver/vacuum interface at first encounter is called J_{el}. We tentatively assume a return rate of these electrons to the Al side into the initial starting state, because this is the only available state. The probability for this process is modelled by an elastic reflection, p_{el}, at the oxide/silver interface. Further reflections are neglected. One derives easily for the tunnel current J_T

$$J_T = J_0 \cdot \left[1 \left(\frac{J_{el}}{J_0} \right)^2 \cdot_{el} el \right].$$

Electron–electron scattering in Ag at negative tunnel voltages (electron current from Al to Ag) leads to a cascade of secondary electrons and holes in Ag. The secondary hot electrons cannot tunnel to the Al side, because they are below the Fermi level of the Al; however, hot holes can tunnel to the Al, because there are filled electron sites ("empty hole sites") on the Al side. Therefore after localization and energy relaxation a charge of more than one electron per primary electron

may contribute to the tunnel current, which is measured in the outer circuit of the MIM junction as a transport current involving only Fermi electrons at the Fermi levels of the circuit. In the ballistic model this effect can be tackled by renormalizing J_0. Diffuse elastic scattering at the silver surface will, of course, change p_{el}, but not the secondary cascade. If inelastic scattering in the surface zone can be neglected, the renormalized J_0 will not depend on p_{el}.

If we try to explain the observed change of J_T by cold deposition on Ag on the junction (see earlier) at $U_T = -1$ V (which is about a factor of 3.1), we may choose the favorable conditions $t_{el} = 1$ and p_{el} varying from 1 to 0, yielding the ratio $\frac{J_{el}}{J_0} \approx 0.9$ after traversing 20 nm of the silver.

This result is very unlikely, since the mean free path of electron–electron interaction is given by Quinn [96] by the following equation (see also Fig. 28):

$$\lambda_{ee} = \frac{1.45 \cdot E_F^{1.5} \cdot E}{\sqrt{\frac{m*}{m} \cdot \arctan\left(\beta^{\frac{-1}{2}}\right) + \frac{\beta^{\frac{1}{2}}}{\beta+1}}} \cdot \frac{1}{(E - E_F)^2}, \qquad (14)$$

with $\frac{m*}{m} = 1.1$ and $\beta = 0.166 r_s$. E and E_F are given in electron volts and λ_{ee} in nanometers.

The mean free path for silver ($E_F = 5.5$ eV, $r_s = 3.08$) is given as an example in Fig. 28.

Accordingly we have to expect a mean free path of only several nanometers for $U_T \sim 2$ V. Only for smaller tunnel voltages $U_T \leq 1$ V do we have mean free paths of above 80 nm.

We therefore propose a model of modulating the dephasing of tunneling states by surface effects.

Model of dephasing at the outer interface of an MIM junction

There are two limiting pictures of tunneling: The usual consideration of the tunneling process between two half spaces (metal 1, aluminium and metal 2, silver, separated by a thin barrier) assumes a free electron approaching the barrier from, for example, the side of metal 1 and tunneling to metal 2 with a usually small transmission amplitude, calculated by the WKB method or directly [95]. The wavefunction of the tunneling electron is continuous; in other words coherence is kept in metal 2 with respect to metal 1. Scattering processes dephasing the coherent state are not considered in the calculations. However tunneling as measured by an external current meter is not complete without the eventual decay of the coherent wavefunction and the localisation of the electron in a new wavefunction restricted to metal 2. In the case that the thickness of the metal 2 electrode exceeds by far the mean free path of the tunneling electron in metal 2 this condition is always fulfilled.

The other limiting picture for a tunneling process in an MIM is the two-well system consisting of two thin
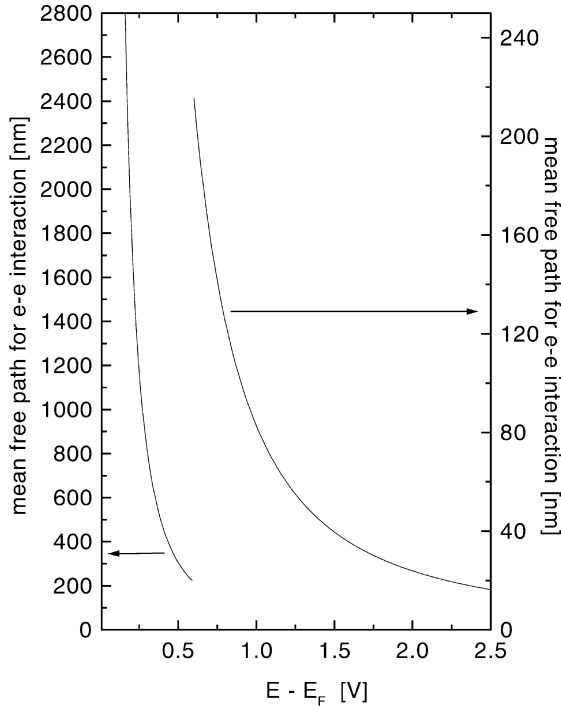
Fig. 28 Mean free path for electron–electron interaction (according to Eq. 14) for silver ($E_F = 5.5$ eV, $r_s = 3.08$) as a function of E–E_F from 0.1 to 2.0 eV (equivalent to tunnel voltage U_T from –0.6 to –2.0 V)
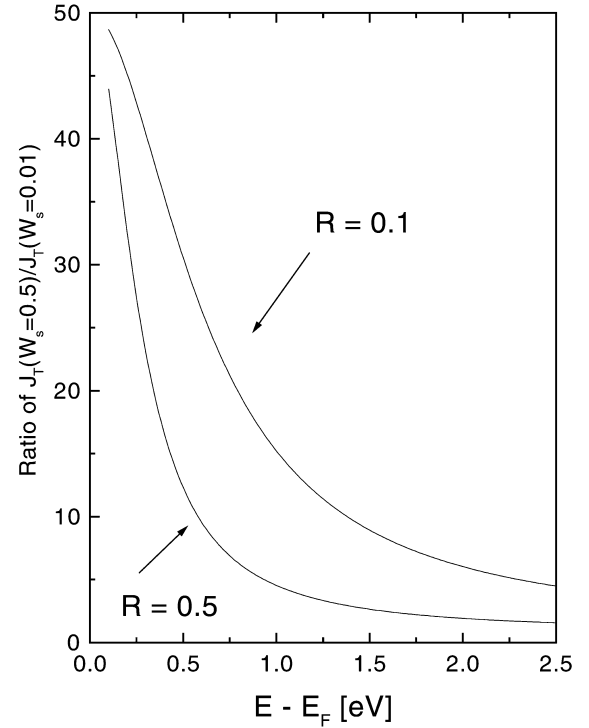

Fig. 29 Ratio of $\frac{J_T(W_s=0.5)}{J_T(W_s=0.01)}$ (tunnel current with strong dephasing at the surface/tunnel current with weak dephasing at the surface) versus $E - E_F$ for two parameters of R

films. Without the scattering process, the electron originally on side 1 oscillates with a time period given by the tunnel barrier and the electron energy coherently between side 1 and side 2 (like in covalent bonding of a H_2^+ ion); it never settles on side 2.

As a more realistic description we assume coherently evolving electron states starting in well 1 (Al) and extending at $t > 0$ into well 2(Ag). Dephasing processes will eventually weaken the probability of finding the electron in the coherent state and will localize the electron as a hot electron in well 2. The most important dephasing processes are electron–electron scattering in the bulk of silver or aluminium and elastic scattering by disorder of the interfaces, where only the external silver surface can be influenced experimentally. The mean free path of electron–phonon interaction is larger than λ_{ee} at the given electron energies and will be neglected. Probably the inelastic scattering at the interfaces is less important than the elastic scattering, but this plays no role in the present case.

The mean free path, λ_{ee}, in electron–electron Coulomb scattering is calculated with electrons normalized to a probability of 1 within the same volume. This is different in our case, where we are, for instance, interested in tunneling from Al to Ag and the scattering of the electron in the coherent state with the electrons in the Fermi sea of well 2 (Ag). This leads formally to an increase of the mean free path, λ_{ee}, in well 2 to $\frac{\lambda_{ee}}{R}$, where R is the probability of finding the electron in state j_{1-2} in well 2(Ag).

Assuming the tunnel current is controlled by two dephasing processes, electron–electron scattering in the bulk and elastic diffuse scattering probability W_s ($0 < W_s < 1$) at the outer surface of the silver electrode, the corresponding simple approach to the tunnel current is

$$J_T \propto J_0 \cdot \left(\left(1 - e^{-\frac{R \cdot d_{Ag}}{\lambda_{ee}}} \right) + W_S \cdot e^{-\frac{R \cdot d_{Ag}}{\lambda_{ee}}} \right), \quad (15)$$

where J_0 is the tunnel current within an infinitely thick top silver electrode and d_{Ag} the thickness of the silver film top electrode. Note that for small d_{Ag} and $W_s = 0$ the tunnel current is very small, but can be significantly controlled by increasing W_s. R is a function of J_∞ (given by the barrier), the ratio $\frac{d_{Ag}}{\lambda_{ee}}$ and of W_s, which we do not know how to calculate.

For an explanation of the surface influence on the tunnel current we choose the surface factor W_s in Eq. (15) to be 0 and 0.5. For simplification, in the present work we consider the ratio

$$\frac{J_T(W_S = 0.5)}{J_T(W_S = 0.01)},$$

for which J_0 does not need to be calculated. In Fig. 29 we plotted this ratio versus $E - E_F$ for $R = 0.1$ and $R = 0.5$.

Figure 29 reveals that the tunnel current becomes more and more "surface determined" at low tunnel voltages ($-e \cdot U_T = E - E_F$). This is reasonable, because

the mean free path, λ_{ee}, increases [approximately proportional to $\frac{1}{(E-E_F)^2}$, see Eq. (14)] and consequently bulk dephasing becomes less important at decreasing $(E-E_F)$. With increasing W_s the value of R decreases. This adds further to the determination of J_T by surface dephasing, see the curve for $R = 0.1$ in Fig. 29.

We assign the increase of W_s to the deposition of unordered silver on smooth silver top electrodes, both in UHV and in the electrolyte to increasing dephasing by elastic scattering in the disordered surface layer. It is clear that the modulation of the tunnel current, I_T, by variation of the probability, W_s, of dephasing at the surface involves only the primary hot electrons; secondary hot electron states may also dephase at the surface, but they do not contribute to I_T.

In the case of the results described earlier the surface dephasing factor W_s is assigned to elastic scattering at the disordered silver surfaces.

Modulation of the internal tunnel current by faradaic reactions at the top electrode

Electron emission into the electrolyte

As a test we used the lower edge of the electronic conduction band in the electrolyte, called the level of the dry electron state (here called the photoemission threshold PE) as an electron acceptor.

The tunnel current of an Al/AlO$_x$/Au system is plotted as a three-dimensional plot versus the tunnel voltage and the electrode potential in Fig. 30.

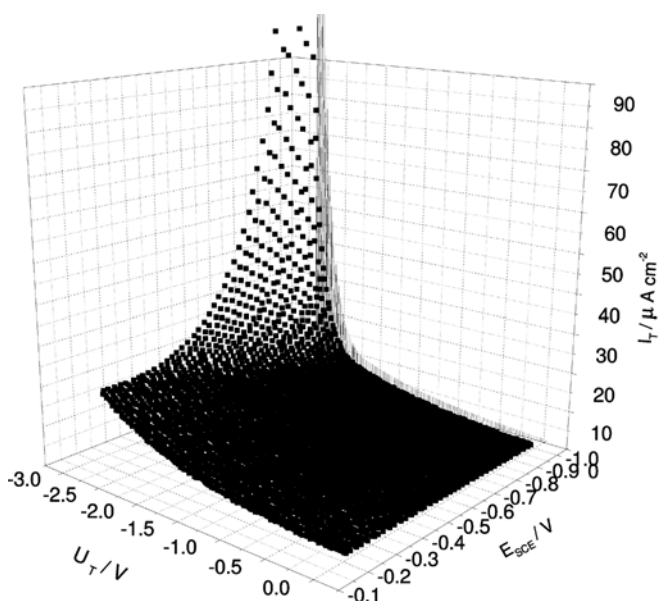One can see clearly that the tunnel current, I_T, increases drastically near $U_T=-2.5$ V and $E_{SCE}=-0.9$ V,

where the tunneled electrons from the Al may reach the dry electron state PE in the electrolyte situated at a potential $E_{SCE}(PE)$ given by

$$e \cdot E_{SCE}(PE) + e \cdot U_T = -3.3 \, \text{eV}.$$

Interestingly the electron emission current into the electrolyte taken under the same conditions ($U_T = -2.7$ V, $E_{SCE} = -1.0$ V) increases absolutely only by about 1.5 µA cm^{-2}, see Fig. 31. This behavior of the tunnel current and the electrode current allows two statements:

- The tunnel current (current from the Al base electrode to the Au top electrode in this case) can be clearly modulated by the electrode potential which is applied at the gold surface.
- Only a fraction (in the present case about 30%) of the tunnel current from the Al through the oxide and to the Au top electrode continues into the dry electron states. (This "yield" is much higher than in Fig. 11. In Fig. 11 a thinner oxide with 2.5-nm thickness was used, causing a much higher tunnel current, several milliamps. In that case, scavenger reactions which follow the process of hot electron injection into the PE may become determinant.)
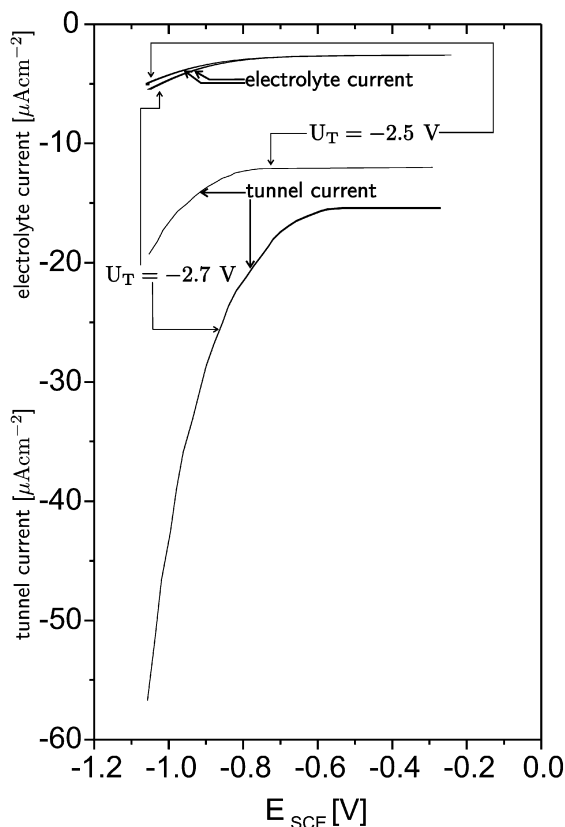

Fig. 30 Three-dimensional plot for the tunnel current of a smooth Al/AlO$_x$/Au (anodic oxide, $d = 3.2$ nm) tunnel junction versus the tunnel voltage and the electrode potential. Sample area $A = 0.1$ cm^2

Fig. 31 Electrolyte current (*two upper curves*) and tunnel current (*two lower curves*) versus electrode potential for two different tunnel voltages, taken with the same tunnel junction as in Fig. 30. Sample area $A = 0.1$ cm^2

Therefore the modulation of I_T is assigned partly to dephasing by elastic scattering of the coherent state φ_{1-2} by the (compared to the crystal) disordered Helmholtz layer. When the energy of φ_{1-2} reaches the energy of level PE (see Fig. 10) this state will extend into the Helmholtz layer up to and beyond the average position of the cores of the water molecules in the relatively disordered Helmholtz layer, see Fig. 34. Note that we do not need to involve any atomic scale roughness of the silver electrolyte interface for our explanation.

Dependence of the tunnel current on the potential for activated surfaces

As already mentioned, the HER by hot electrons needs weak activation. In this case, the tunnel current at constant tunnel voltage also increases considerably at the onset of the HER. First we plot the tunnel current versus the tunnel voltage of an Al/AlO$_x$/silver system with an activated silver top electrode in a buffered acetate electrolyte at electrode potentials $E_{SCE} = -0.8$ V, $E_{SCE} = -1.0$ V, and $E_{SCE} = -1.2$ V, see Fig. 32.

There is a big dependence on the electrode potential, E_{SCE}. The dependence of the tunnel current on the electrode potential at constant tunnel voltage is shown in Fig. 33. There is almost no hysteresis. Further there is no dependence on the scan velocity from 20 up to 500 mV s^{-1}. (This means that the tunnel current at constant tunnel voltage is clearly influenced by the electrode potential and not by accumulated reaction products of the HER.) Since the increase of the tunnel current is observed in the range of the hydrogen evolution by hot electrons, we have to discuss the assignment of the modulation of I_T to this faradaic reaction. Here the comparison of I_T and I_{el} as a function of E is very helpful.

A conventional cyclovoltammogram is shown in Fig. 33, while the tunnel voltage is set to $U_T = -2.4$ V. We also plotted the tunnel current on the same scale. The tunnel current increase due to the change of electrode potential of about 6 mA cm^{-2} exceeds the electrolyte current due to faradaic reactions of about 1.4 mA cm^{-2} by about 400%, see Fig. 33.

Therefore we have to assign at least the bigger part of the modulation of I_T to a nonfaradaic process. We propose like before dephasing by atomic scale roughness, but in this case it increases with cathodic potential. This increase is caused by the lowering of the level PE and the corresponding further penetration of the hot electron into the electrolyte with increasing cathodic potential, as shown schematically in the upper part of Fig. 34 for a smooth surface. This is analogous to the curves for a smooth Ag(111) electrode and finite negative U_T in Fig. 20. The ASR is characterized in the lower part of Fig. 34 by a silver adatom on an Ag(111) surface. The absolute probability amplitude of the coherent state φ_{1-2} at the adatom site will increase at increasing
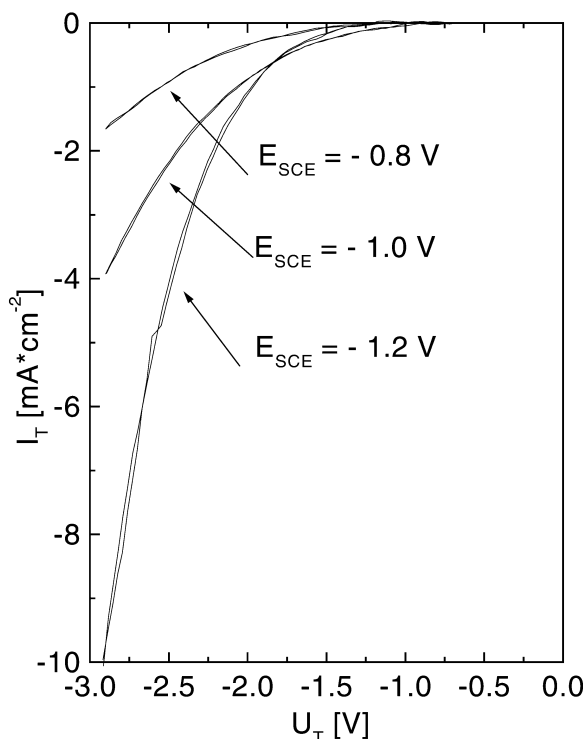

Fig. 32 Cyclic voltammogram plots of tunnel current I_T versus tunnel voltage U_T of an Al/AlO$_x$/Ag junction with activated silver top electrode in 0.9 M acetate buffer electrolyte (50% water, 50% ethylene glycol) taken at different electrode potentials E_{SCE}
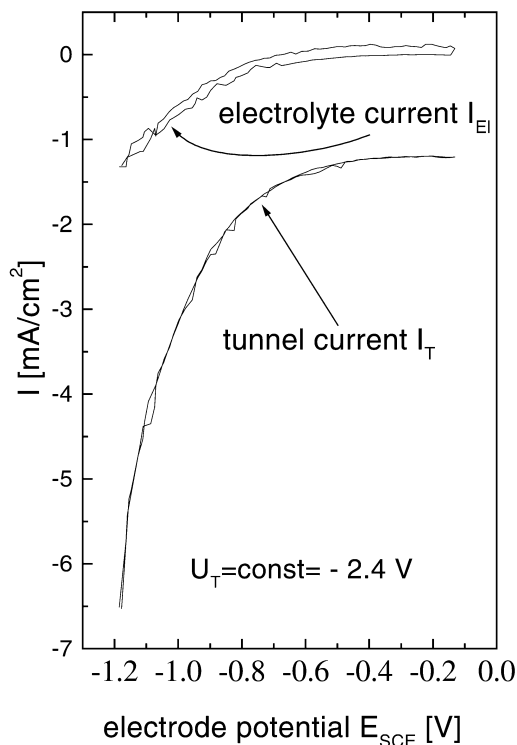
Fig. 33 Tunnel current at constant tunnel voltage of $U_T = -2.5$ V as a function of the electrode potential in acetate buffer electrolyte (50% water, 50% ethylene glycol) $\frac{dE}{dt} = 50$ mVs^{-1}. Note that the scans in the negative and positive directions are very similar

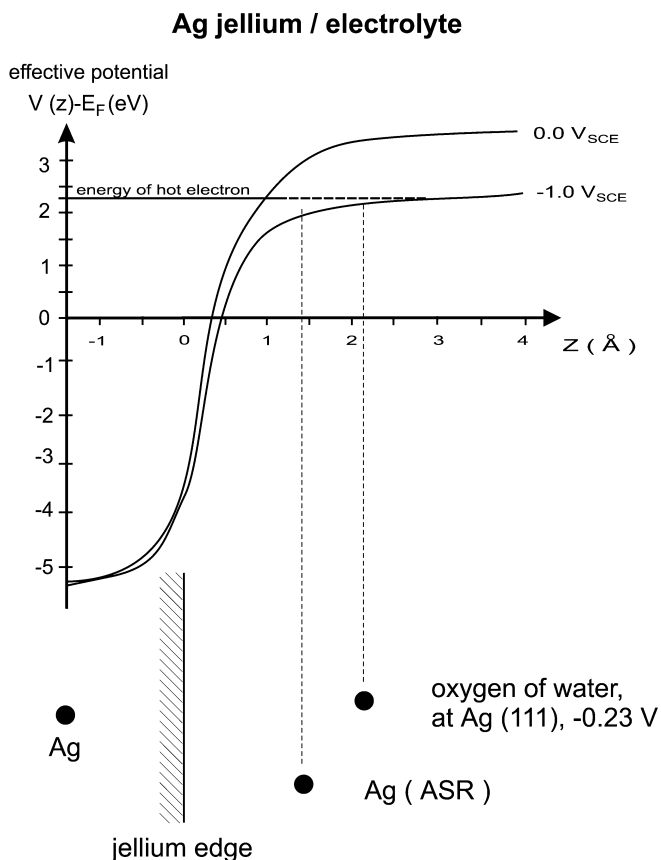## Ag jellium / electrolyte

effective potential
$V(z)-E_F$ (eV)

Fig. 34 *Top*: schematic representation of the effective potential $V(z)$ for electrons at the silver–jellium/electrolyte interface for $E_{SCE} = 0.0$ and –1.0 V, as afunction of the distance z from the jellium edge. $V(z)$ has been drawn in qualitative agreement with the effective potential for jellium/ultrahigh vacuum surfaces in Ref. [97]. $V(z)$ at large z corresponds to the level PE in Fig. 10. *Bottom*: position of the cores of the silver atoms at the Ag(111) surface, where the absolute distance from the jellium edge is half the nearest-neighbour distance in bulk silver. The left ($z < 0$) core typifies a smooth (111) terrace, the right core ($z > 0$) an adatom on the terrace as an example of atomic scale roughness (*ASR*). The distance between the cores of the Ag surface atoms and the oxygen cores of the inner water layer in the Helmholtz layer at a cathodic potential at smooth Ag(11) has been taken from X-ray scattering experiments [78]

cathodic potential and accordingly a higher probability of scattering by atomic scale roughness and an increase of the factor W_s in Eq. (15) is expected.

Sensorics with MIM junctions

MIMs have the unique property of probing a metal–vacuum, metal–gas or metal–electrolyte interface "from the metal side" (from "inside"), via changes of the tunnel current in the following ways:

- The internal current of hot carriers released at the surface contributes to the tunnel current, for instance, in nonadiabatic surface reactions, for example, the oxidation of an adsorbed layer of hydrogen, see earlier and Ref. [43].
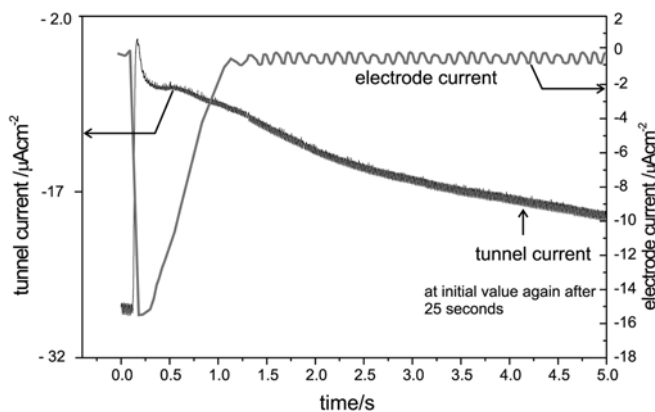

Fig. 35 Change of the tunnel current during injection at the time of ca. 1.1 s of the electrolyte current (*right scale*) during and after the injection of ethanol in the electrolyte 50% water/50% ethylene glycol and 0.05 M KClO$_4$ in front of the MIM, at an electrode potential of E_{SCE} = –0.9 V and a tunnel voltage of –1.0 V. The valve was open for 20 ms. Taken from Ref. [98]

- The tunnel current is changed by surface disorders at the silver/UHV and silver/ electrolyte interfaces (see Fig. 27), by the electrode potential at silver electrolyte interfaces and maybe also by molecular adsorption, according to some results under UHV conditions. Both points demonstrate the potential of MIM junctions for chemical and electrochemical sensing and maybe also, indirectly, for sensing of disorder caused by friction.

Chemical sensing was demonstrated by time-defined injection of ethanol into the electrolyte consisting of 50% water/50% ethylene glycol and 0.05 M KClO$_4$ [98]. A micro inert valve (Lee company type LFRX) was positioned with its exit channel perpendicular to the MIM at a distance of about 3–5 mm. The opening times of the valve could be chosen from 20 ms onwards; the quantity of methanol injected through the valve into air was about 3 ml s^{-1}. Nothing is known on the stream velocity distribution within the electrolyte but the velocities probably do not exceed 1 m s^{-1}.

Figure 35 shows the changes of the electrode current and the tunnel current after ethanol injection with an opening time of 20 ms, the tunnel voltage and the electrode potential being stabilized at –1.0 and –0.9 V_{SCE}, respectively. The electrode current changes in the first 200 ms from a small negative value to –17 μA cm^{-2} and then in about 1 s to about the initial value of around 1 μA cm^{-2}. The oscillations of the electrode current in Fig. 35 are caused by the nitrogen bubbling of the electrolyte. The concomitant change of the tunnel current is from –28 μA cm^{-2} within the first 200 ms to only –5 μA cm^{-2}, returning to the initial value after about 25 s [98]. The transients are most pronounced at the electrode potential of –0.9 V_{SCE}, see Fig. 36, whereas they are much weaker at –0.3 V_{SCE}.

The high response to injections at cathodic potentials seems to be analogous to the changes of the tunnel current with electrode potential at constant tunnel
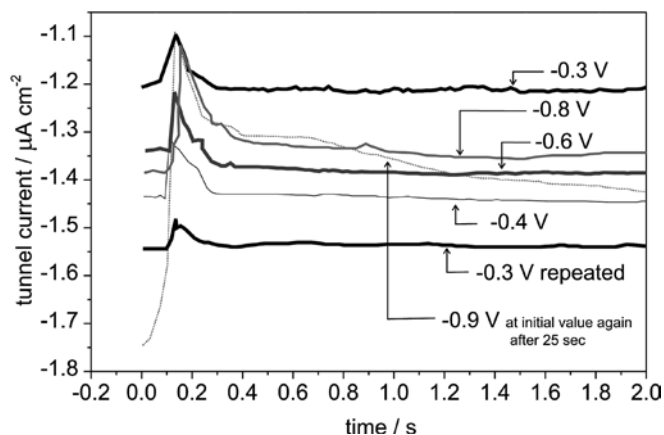
Fig. 36 Like Fig. 36, but at the indicated electrode potentials. Time sequence of measurements at $V_{SCE} = -0.3$ (tunnel current I_T near -1.55 μA), -0.4, -0.6, -0.8, -0.9, and -0.3 (tunnel current I_T near -1.2 μA). Taken from Ref. [98]
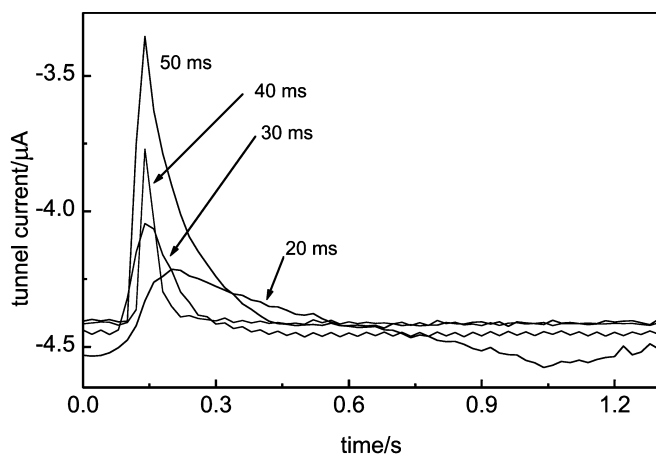

Fig. 37 Change of tunnel current during and after the injection of ethanol in the electrolyte in front of the MIM, at electrode potential $E_{SCE} = -0.85$ V and tunnel voltage $U_T = -0.5$ V. The valve was open for the indicated times. Taken from Ref. [98]

Fig. 38 Change of tunnel current during injection at the time of ca. 1.19 fo the electrolyte current (*right scale*) during and after injection of the electrolyte 50% water/50% ethylene glycol and 0.05 M $KClO_4$ into the same electrolyte in front of the MIM at electrode potential $E_{SCE} = -0.9$ V and a tunnel voltage of -0.5 V. The valve was open for 20 ms. Taken from Ref. [98]

the transient in the tunnel current was like the short spike sitting on the long-time transients during heterogeneous injection, Fig. 38.

There seem to exist rather delicate processes in the Helmholtz layer, both depending on the surface concentration and perhaps also on the transient orientation of adsorbates by the stagnation pressure during injection with an average stream velocity of the order of 1 ms^{-1} not exceeding that of the river Rhine flowing through Dusseldorf.

voltage, see, for instance, Fig. 32, where at a tunnel voltage of -1.0 V the tunnel current only reacts at cathodic electrode potentials.

Therefore we tentatively assign the transients beyond 0.5 s to the adsorption and the desorption processes of ethanol in the Helmholtz layer and the high "susceptibility" of I_T to such changes in the double layer at negative potentials $E_{SCE} < -0.8$V. The structure in the transients within the first 200 ms depends on the injection times, see Fig. 37, which could mean that the macroscopic streaming of the electrolyte plays a role as well. To study this, it seemed appropriate to inject the same electrolyte rather than methanol (homogeneous injection). Care was taken to degas the electrolyte both in the bath of the MIM and in the pumping system. Interestingly the transient of the electrode current in the homogeneous injection was of the same order as in the heterogeneous methanol injection, but simply speaking
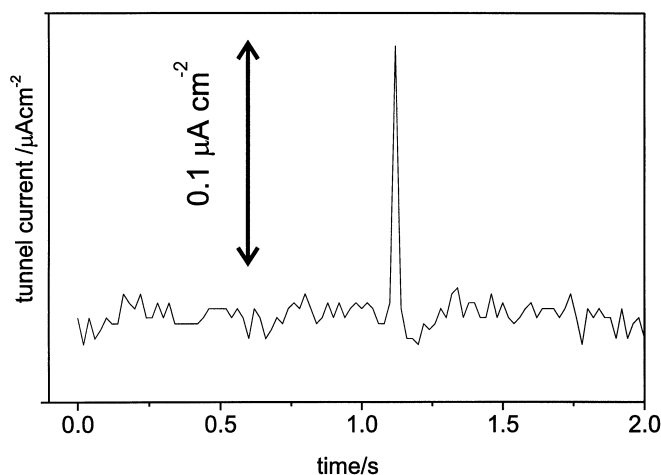
Outlook

MIM tunnel junctions have several unique features. They allow "surface photochemistry without photons", because the intermediate hot electrons in photochemistry are created by tunneling into the top electrode. Though MIM junctions are slow devices, they can deliver information on the energetic distribution of the electronic excitations involved in the initial coherent state and discriminate between surface and bulk excitations. Because hot electrons emitted in surface reactions can be monitored, MIM junctions can strongly contribute to the study of nonadiabatic surface reactions. This field is not easily accessible to other methods. We also see a practical aspect in sensorics, as the tunnel current depends on conditions at the outer surface of the top electrode of the MIM junction. They may act simultaneously both as a sensor and a transducer.

All these statements, for which we have given examples in this article for interfaces with electrolytes, apply for interfaces with gases as well as for UHV. Future applications may, for instance, involve hot-electron-induced desorption, genuine optical surface absorption, nonlinear optical phenomena, state- and time-resolved

surface reactions, surface interactions of metastable species, and maybe some not yet anticipated uses in sensorics.

References

1. Bockris J, Conway B (1980) Comprehensive treatise of electrochemistry, Vol 1, Plenum, New York
2. Schmickler W (1983) Chem Phys Lett 99:135
3. Schmickler W, Henderson D (1986) J Chem Phys 85:1650
4. Kornyshev A, Schmickler W, Vorotyntsev M (1982) Phys Rev B 25:5244
5. Schmickler W, Henderson D (1986) Prog Surf Sci 22:323
6. Schultze J, Stimming U (1975) Z Phys Chem 98:285
7. Liebsch A (1998) Electronic excitations at metal surfaces. Plenum, New York
8. Steinmann W, Fauster T (1995) In: Dai HL, Ho W (eds) Laser spectroscopy, photochemistry on metal surfaces. World Scientific, Singapore, chap 5, p 764
9. Osgood RM, Wang X (1998) Solid State Physics 51:2
10. Bauer M, Pawlik S, Aeschlimann M (1997) Phys Rev B 55:10040
11. Hertel T et al (1994) Surf Sci 317, L 1147
12. Gurevich YV, Pleskov YV, Rothenberg ZA (1980) Photoelectrochemistry. Consultants Bureau, Singapore
13. Sass J (1980) Surf Sci 101:507
14. Furtak T, Kliewer K (1978) Solid State Comm 26:177
15. Furtak T, Kliewer K (1982) Comments Solid State Phys 10:103
16. Feulner F, Menzel D (1995) In: Dai HL, Ho W (eds) Laser spectroscopy, photochemistry on metal surfaces. World Scientific, Singapore, chap 16, p 627
17. Wetzig D et al (1998) Surf Sci 232:402–404
18. Hasselbrink E (1994) Appl Surf Sci 34:79–80
19. Ho W (1995) In: Dai HL, Ho W (eds) Laser spectroscopy, photochemistry on metal surfaces. World Scientific, Singapore, chap 24
20. Zhou XL, White JM (1995) In: Dai HL, Ho W (eds) Laser spectroscopy, photochemistry on metal surfaces. World Scientific, Singapore, chap 25
21. Zimmermann F, Ho W (1996) In: Dai HL, Ho W (eds) Surface photochemistry. Wiley, New York, chap 2
22. Decker F (1993) Electrochim Acta 38:1
23. Kostecki R, Augustynski J (1993) J Appl Electrochem 23:567
24. Goldmann A (1995) Electronic surface, interface states on metallic systems. World Scientific, Singapore, p 35
25. Richmond GL, Robinson JM, Shannon VL (1988) Prog Surf Sci 28:1
26. Pettinger B, Bilger C, Lipkowski J, Schmickler W (1998) Interfacial electrochemistry. Dekker, New York, chap 22
27. Pluchery O, Tadjeddine M, Flament J, Tadjeddine A (2001) Phys Chem Chem Phys 3:3343
28. Höfer U (1999) Appl Phys B 68:383
29. Funtikov A, Sigalaev S, Kazarinov V (1987) J Electroanal Chem 228:197
30. Bruckbauer A, Otto A (1998) J Raman Spectrosc 29:665
31. Misewich JA, Heinz T, Newns D (1962) Phys Rev Lett 68:3737
32. Downes A, Guaino P, Dumas P (2001) Appl Phys Lett 80:380
33. Bartels L et al (1998) Phys Rev Lett 80:2004
34. Schmickler W (1995) Surf Sci 335:416
35. Schmickler W (1993) Surf Sci 295:43
36. Vetter K, Schultze J (1973) Ber Bunsenges Phys Chem 77:945
37. Kohl P, Schultze J (1973) Ber Bunsenges Phys Chem 77:953
38. Schmickler W, Schultz J (1986) Mod Aspects Electrochem 17:357
39. Diesing D, Janssen H, Otto A (1995) Surf Sci 289:331–333
40. Schatteburg S, Diesing D, Otto A (2000) Appl Phys B 70:573
41. Diesing D, Kritzler G, Otto A (2003) In: Thurgate S, Wandelt K (eds) Solid liquid interfaces, macroscopic phenomena, microscopic understanding. Topics in applied physics 85. Springer, Berlin Heidelberg New York, pp 365–421
42. Fowler RH, Nordheim L (1928) Proc Roy Soc London Ser A 173
43. Kritzler G (2001) Dissertation. Universität Düsseldorf
44. Otto A (file available upon demand)
45. Borisov A, Kazansky A, Gauyacq J (1999) Phys Rev B 59:10935
46. Gadzuk JW (1996) Phys Rev Lett 76:4234
47. Otto A, Diesing D, Janssen H, Hänisch M, Lohrengel MM, Rüße S, Schaak A, Schatteburg S, Körwer D, Kritzler G, Winkes H (1997) In: Roberts MW (eds) 'Interfacial Science', Chapter 7, Blackwell Science (Reprints available), pp 163–193
48. Gadzuk JW (1997) J Vac Sci Technol A 15:1520
49. Diesing D, Hassel AW, Lohrengel MM (1999) Thin Solid Films 342:283
50. Hänisch M, Otto A (1994) J Phys Condens Matter 6:9659
51. Guedes M, Slayman K, Jain G (1979) IEEE Journal Quantum Electron 475
52. Diggle J, Downie T, Goulding C (1969) Chem Rev 69:365
53. Hassel A, Seo M (1999) Electrochim Acta 44:3769
54. Hassel A, Diesing D (2002) Electrochem Commun 4: 1
55. Hassel A, Diesing D (2002) Thin Solid Films 414:296
56. Diesing D, Rüsse S, Otto A, Lohrengel MM (1995) Ber Bunsenges Phys Chem 99:1402
57. Simmons J (1963) J Appl Phys 34:1793
58. Simmons J (1964) J Appl Phys 35:2655
59. Duke C B (1969) Tunneling in solids. Academic, New York, p 53
60. Politzer B (1966) J Appl Phys 37:279
61. Ashcroft N, Mermin N (1976) Solid state physics. Holt Saunders, Philadelphia, chap 18, p 364
62. Hickmott T (2001) J Appl Phys 89:5502
63. Staib A, Borgis D (1995) J Chem Phys 103:2642
64. Barker G, Gardner A (1973) J Electroanal Chem 47:205
65. Benderskii V et al (1974) J Electroanal Chem 56:325
66. Diesing D, Kritzler G, Otto A (1997) Ber Bunsenges Phys Chem 101:762
67. Gerischer H (1973) Ber Bunsenges Phys Chem 77:771
68. Curtis M, Walker I (1992) J Chem Soc Faraday Trans 88:2805
69. Rowntree R, Parenteau L, Sanches L (1991) J Chem Phys 94:8570
70. Sass JK, Gerischer H (1978) In: Feuerbacher B (ed) Photoemission, the electronic properties of surfaces. Wiley, New York, chap 16
71. Meyer E (1973) Dissertation. Technische Univeirtät München
72. Pleskov YV, Rothenberg ZA (1969) J Electronal Chem 20:1
73. Körwer D (1992) In: Kiefer W, Cardona M, Schaak G, Schneider FW, Schrötter HW (eds) Proc. XIII International Conference on Raman Spectroscopy. J. Wiley & Sons, p 648
74. Diesing D (1996) Dissertation. Heinrich-Heine-Universität Düsseldorf
75. Diesing D, Kritzler G, Otto A (1997) In: Kornyshev A, Tosi M, Ulstrup J (eds) Electron, ion transport in condensed media. World Scientific, Singapore, p 257
76. Tölle R (2003) Dissertation. Universität Düsseldorf
77. Diesing D, Winkes H, Otto A (1997) Phys Stat Sol A 159:243
78. Toney ME et al (1995) Surf Sci 335:326
79. Pecina B, Schmickler W (1997) J Electroanal Chem 431:47
80. Eckhardt H, Fritsche L, Noffke J (1984) J Phys F 14:97
81. Noffke J, private communication
82. Otto A, Reihl B (1990) Phys Rev B 41:9752

83. Reetz M, Quaiser S (1995) Angew Chem Int 20:34
84. Winkels S (2000) Dissertation. Universität Düsseldorf
85. Pfeiffer B, Thyssen A, Schultze JW (1989) J Electroanal Chem 260:393
86. Clavillier J (1980) J Electroanal Chem 107:1190
87. Stermann M (2001) Diplomarbeit Universität Düsseldorf
88. Rolandi M, Scott K, Wilson EG, Meldrum FC (2001) J Appl Phys 89:1588
89. Graf H, Vancea J, Hoffmann H (2002) Appl Phys Lett 80:1264
90. Bardeen J (1961) Phys Rev Lett 6:57
91. Josephson B (1967) Advan Phys 163:341
92. Kaiser L, Bell W (1988) Phys Rev Lett 60:1406
93. Prietsch M (1995) Phys Rep 253:163
94. Otto A (2003) Europhys Lett (in press)
95. Tonscheidt A (1990) Diplomarbeit Universität Düsseldorf
96. Quinn JJ (1962) Phys Rev 126:1453
97. Jennings PJ, Jones R, Weinert M (1988) Phys Rev B 37:6113
98. Nolting D (2002) Diplomarbeit Universität Düsseldorf